The efficient inclusion of rotation-induced inertia effects in a shaft-blisk assembly model using zero-speed modes

Document Version
Accepted author manuscript

[Link to publication record in Manchester Research Explorer](#)

The Efficient Inclusion of Rotation-Induced Inertia Effects in a Shaft-Blisk Assembly Model using Zero-Speed Modes

Mohamed Elsayed Mohamed[a,b]*, Philip Bonello[a]

[a] School of Mechanical, Aerospace and Civil Engineering, University of Manchester, Manchester, United Kingdom
[b] Department of Mechanical Design and Production, Faculty of Engineering, Cairo University, Giza, Egypt

*Corresponding author.
 E-mail address: mohamed.mohamed-2@manchester.ac.uk (M. E. Mohamed)

ABSTRACT

A successful design of rotating shaft-bladed disk ("blisk") assemblies requires the facility to reliably predict the resonance speeds, which must be avoided during operation to avoid failure. Rotation-induced inertia effects (centrifugal stiffening, spin softening, Coriolis forces and gyroscopic moments) can cause significant variation of the modal frequencies with speed. A review of the state-of-the-art highlights the need for a methodology that can efficiently include all rotation-induced inertia effects in a generic shaft-blisk system. The novel contribution of this paper is a methodology to include such effects in a generic shaft-blisk system, using zero-speed finite element (FE) modal data, without the need for additional FE analysis at each speed, or the derivation of equations from first principles. This contribution is motivated by the need to upgrade an existing blisk simulator designed to generate blade tip timing (BTT) data for the development and validation of BTT algorithms. Rotational effects are added as discretised "external" excitations to the modal equations, which remain based on the zero-speed modes. The method is progressively validated on six examples, using results from the literature and commercial FE rotordynamics software, to demonstrate its accuracy and high efficiency of computation for both Campbell diagrams and forced response.

Keywords

Bladed Disk Assembly; Rotational Effects; Finite Element Analysis; Modal Analysis; Campbell Diagrams

1. INTRODUCTION

Shaft-blisk ("bladed disk") assemblies in turbomachinery often fail due to fatigue when they are exposed to excessive vibration in the resonant condition. To avoid such failure, it is of importance to accurately predict the vibration modes during the design stage. The deformations of the shaft, disk and blades are always to be coupled to some extent [1]. However, owing to the complexity of the problem, the majority of the early studies have been limited to analyses of individual elements, which is appropriate for cases where the fundamental natural frequency of the individual element is much lower than that of the other elements. The high speed, light weight, and large scale of modern turbomachinery have increased the importance of the higher critical speeds of such systems. This has consequently increased the need to study the effect of rotation-induced inertia effects on the vibration characteristics. These effects are: centrifugal stiffening, spin softening, Coriolis forces and gyroscopic moments [2]. In the absence of such effects, the natural frequencies of the shaft-blisk system are independent of speed. Rotation-induced inertia effects result in the splitting of certain natural frequencies with increasing speed on the Campbell diagram (natural frequencies *vs* speed graph) [3].

The early analysis of blades was based on one-dimensional beam theory. Later on, rotation-induced inertia effects were included in the beam model [4]. For beams, these effects come from centrifugal and Coriolis forces. Such effects were neglected in some studies [5–8] and considered in others [9–11]. For shaft-blisk assemblies, the accurate modelling of rotation effects requires consideration of disk flexibility. Preliminary studies based on simple models have shown the possible effect of disk flexibility on the critical speeds of rotating solid shafts

2

[12–15]. Crawley et al. [16] showed that the blade modes with one nodal diameter dynamically couple to the rigid body whirling motion of the shaft-disk system. Shahab and Thomas [17] showed that the transverse movement of the shaft can excite the backward or forward whirling of the shaft-blisk system.

In order to get an accurate prediction of the dynamic characteristics of turbomachinery, one ought to model a shaft-blisk system as an assembly, in which all the elements are dynamically coupled together [18]. Methods such as finite element (FEM), dynamic stiffness (DSM), assumed modes (AMM), and experimental methods, or combinations of these methods were used for modelling and analysis of rotating assemblies including the flexibility and dynamic couplings between different components [18–22].

In case of a single nodal diameter whirling mode of the blisk, a pitching force/moment is exerted on the shaft which couples the bending behaviour of the blisk to the shaft whirl through gyroscopic effect, resulting in forward and backward whirl modes [23]. The gyroscopic effects, rotary inertia, and shear deformation of the shaft can be ignored relative to those of the blisk at intermediate shaft speeds [23].

Some early studies, such as the one of Suyehiro, assumed that the gyroscopic load is acting on the mid-plane of a stationary disk [24]. Dopkin and Shoup [12] observed that the disk bending modes with one nodal diameter produce a net moment on the shaft and therefore coupled with the shaft flexural modes through gyroscopic effect. In their study, the shaft was modelled as lumped mass segments, while constant thickness plate elements (rings) and concentrated mass elements were used to model the disk. Many other studies considered the gyroscopic effects of one or more components such as [1,2,25,26]. A new dynamic model of a rotor/rigid disk/blade system was presented in 2015 by Ma et al. [2]. The model considered the gyroscopic effects of the disk and shaft, the Coriolis forces, centrifugal stiffening, and

spin softening of the blades, in addition to both the lateral and torsional deformations of the shaft. The blades were modelled using Timoshenko beam elements. The equations of motion were derived by using Hamilton's principle and the assumed mode method. The analytical model was validated against both the finite element model by *ANSYS* FE software and experimentally. The centrifugal stiffening and spin softening effects were included in the *ANSYS* model stiffness matrix by using pre-stressed modal analysis which requires a separate analysis at each speed based on a static analysis.

The trend towards increased efficiency at higher speeds has led to larger blades and stronger stagger angles, which generate large centrifugal and Coriolis forces [26]. Some early studies ignored the Coriolis effects since they were limited to small motions or to beams that are rigid in bending except at disk connection [27]. Krupka and Baumanis [28] found that both shear deformation and rotary inertia should be included in the analysis, as they result in changes of about 4% to 8% in first and second natural frequencies at high speeds. Sisto et al. [29] showed with high accuracy that the Coriolis forces alter the stability of the blades.

A discrete system representation, at which the blade is divided into a number of segments has been employed in some studies [26, 29]. This facilitates the inclusion of Coriolis forces, shear and inertia effects. Xin and Wang found that the maximum frequency split due to Coriolis effects occurs for single nodal diameter modes [31]. A new test rig was developed in 2015 by Ruffini et al. [32] to study the Coriolis effects on blisk-shaft assemblies, and to provide validation data for the available numerical methods. The effect of Coriolis forces on the forced response of mistuned bladed-disk systems was studied by Kan et al. [33].

Rotating cantilever beam models have been used for turbomachinery blades. The vibration characteristics of rotating beams vary significantly with the increase in speed. One of the factors responsible for this variation is the centrifugal inertia force, which causes a significant

stretch in the blades, resulting in a change in the bending stiffness. This is an example of geometric stiffening [34]. Ramamurti and Kielb [35] used the stress smoothing technique in which the rotational stresses were first computed and then used to update the stiffness matrix, which is then used in the eigenvalue analysis. Banerjee derived the dynamic stiffness matrix of the rotating beams including the effect of axial force for both Euler-Bernoulli and Timoshenko beam elements [36,37] and later for tapered beams [38]. According to Banerjee, the dynamic stiffness method gives exact solutions for the natural frequencies and mode shapes without making any approximation [38]. A procedure based on the method of variational iteration was presented in 2016 by Chen et al. [39] for the determination of the natural frequencies and mode shapes of rotating Euler-Bernoulli beams. They showed that the procedure is able to predict the frequencies of higher order modes with acceptable accuracy and relatively low number of iteration steps.

The above mentioned studies, concerning centrifugal stiffening of blades, neglected the flexibility of the disk. Other research works have considered centrifugal stiffening, and other rotation-induced inertia effects, in shaft-blisk assemblies. Chun and Lee developed an analytical synthesis and assumed mode method to study the effect of blisk flexibility on the dynamic behaviour of rotor systems, taking into account the Coriolis forces and centrifugal stiffening [18]. The assumed mode method, finite element method, and experimental method have been adopted by Chiu et al. in 2017 [22] in order to explore the dynamic coupling of multi flexible disk rotor system, considering centrifugal stiffening.

The finite element (FE) method is used in several studies in order to cope with the complicated configurations of rotating systems. However, shaft-blisk assemblies including Coriolis effects are rarely modelled and simulated using FE packages [26]. An investigation of different FE software packages has been done by Ruffini et al. [26] in order to examine their capabilities for predicting the dynamic behaviour of rotor systems in case of Coriolis

5

and gyroscopic effects, especially with regard to the frequency splits. The FE packages used were Abaqus v6.11-13, Ansys v12.1, NX Nastran v8.5, and SAMCEF v14.1. Three test cases were presented, and the resulting Campbell diagrams from all software packages for the three cases were compared to each other and to the results from the literature. One of the test cases was the Stodola-Green rotor, which is a classic model in rotordynamics, and has strong frequency splits due to gyroscopic effects. All software predicted the frequency splits correctly, except at high speed in the vicinity of instabilities.

The non-rotational (i.e. zero-speed) mode shapes of the system obtained using FE analysis were used in a modal analysis approach by Khader and Loewy [30] to study the steady-state forced response of a flexible bladed disk supported by a shaft modelled as a massless, flexible cantilever. Although the method represented the motion using zero-speed modes, it required the derivation of the equations of motion (with rotation effects) from first principles via Lagrange's method. This in turn required the laborious derivation of kinetic energy and potential energy expressions. The part of the potential energy contributed by centrifugal stiffening was derived by discretising the centrifugal force at a number of locations along the blade and calculating its local deformation components. The zero-speed mode shapes were used again by Jacquet-Richardet et al. [15] in a modal analysis method that included gyroscopic effects, spin softening, and centrifugal stiffening. The zero-speed modal method of [15] required static analysis for the geometric stiffness matrix (that contains the centrifugal effect) which had to be repeated at each speed. This is similar to the approach used in the *ANSYS* rotordynamics solver [40] and can be computationally expensive (as shown in section 3 of this paper).

The above literature review highlights the need for a methodology that can efficiently include all rotation-induced inertia effects in a generic shaft-blisk system. The novel contribution of this paper is a methodology to include such effects in a generic shaft-blisk system, using

6

zero-speed modal data and without the need for additional FE analysis at each speed or the derivation of equations from first principles (i.e. unlike [15] and [30] respectively).

The contribution of this paper is motivated by the need to upgrade a blisk simulator designed to generate blade tip timing (BTT) data for the development and validation of BTT algorithms [41]. In this simulator, the blisk motion is a superposition of rigid rotation, prescribed steady movement (i.e. non-oscillatory movement like axial float of the shaft), and vibratory movement due to dynamic excitation forces. This latter component of the movement is represented by a modal superposition that uses modal data from the FE model at zero rotational speed. Transformation to modal coordinates is crucial for the efficient operation of the simulator since the effective number of blisk modes required for accurate convergence of the vibration response is typically much less than the number of degrees of freedom of the FE model [41]. In the current version of the simulator (i.e. as in [41]), the modal equations of motion neglect rotational effects. This simulator was first used by the authors in [42] to investigate the effect of steady movement on BTT data. In the same year, independent researchers [43] presented a simulator that was also based on FE-derived system modes. Although the simulator in [43] accommodated gyroscopic/Coriolis effects as an optional input, these were based on a constant gyroscopic matrix (obtained from FE) applicable to a single speed only. The corresponding natural frequencies used in the modal equations included rotational effects but were only applicable for a single speed. Hence, the variation in rotational speed considered in [43] was only around 10%. Using the methodology presented in this paper, the authors' blisk simulator of [41,42] is upgraded to accommodate rotation-induced inertia effects, without speed restriction, by adding them to the modal equations as "external" excitations at discrete locations, so that the modal equations continue to be based on the zero-speed modes. The simulator is also upgraded to include the deflection of the shaft, but the parametric excitation effect introduced by the

consequent in-plane vibration of the blisk centre [44] is not considered. A similar approach appears to have been taken by Ma et al. [2], Chun and Lee [18].

Section 2 starts with an overview of the existing blisk simulator (which neglects rotational effects on the dynamic response). The methodology for adding rotational effects (Coriolis/spin softening; centrifugal stiffening; gyroscopic) is then presented. Since the method requires angular displacement modal data, a method is presented to calculate such data from the translational modal data. This is a one-off computation that is needed when solid elements are used in the FE modal analysis at zero-speed (since such elements use translational degrees of freedom). The procedures for the computation of the Campbell diagram and the forced response are then described, followed by an extension of the analysis to shaft-blisk systems. Section 3 presents and discusses the results of six examples that are validated against results from the literature or from commercial software.

2. MODELLING FOR ROTATIONAL EFFECTS

2.1 Overview of Existing FE-Based Modal Simulator of Blisk System [41]

The description in this section is taken from [41], where rotation-induced inertia effects were neglected and the system consisted of a blisk only (transverse displacement of shaft neglected). If $\mathbf{u}(t)$ denotes the $3N \times 1$ vector containing the instantaneous absolute coordinates of a subset of FE nodes Q_n ($n = 1 \dots N$) covering a certain region (e.g. the tip of a given blade), the simulator computes $\mathbf{u}(t)$ as follows

$$\mathbf{u}(t) = \mathbf{u}^{(\mathrm{rgd})}(t) + \Delta\mathbf{u}^{(\mathrm{off})}(t) + \mathbf{T}_{\mathrm{aug}}\big(\varphi(t)\big)\Delta\mathbf{u}^{(\mathrm{def})}(t) \tag{1}$$

where:

- $\mathbf{u}^{(\mathrm{rgd})}(t)$ represents the *absolute* blade tip positions due to rotation of the blisk as a rigid body (in the absence of deformation and any applied shifting) following a rotation $\varphi(t)$ from a reference angular position of the blisk.

- $\Delta \mathbf{u}^{(\mathrm{off})}(t)$ represents a prescribed steady (non-oscillatory) shift that is used to simulate "dc" bias errors on BTT data generated by the simulator [41].

- $\Delta \mathbf{u}^{(\mathrm{def})}(t)$ represents the response to the applied dynamic excitation forces.

- $\mathbf{T}_{\mathrm{aug}}\big(\varphi(t)\big)$ is a matrix that transforms displacements in a rotating coordinate frame to displacements in an inertial frame following a rigid rotation $\varphi(t)$.

Since $\Delta \mathbf{u}^{(\mathrm{def})}(t)$ is superimposed on the rigid body rotation and the prescribed steady shift, it is determined by considering the dynamic response of the non-rotating system in a fixed reference angular position. The elements of $\Delta \mathbf{u}^{(\mathrm{def})}(t)$ are calculated using a modal transformation based on the first H undamped modes of vibration of the *non-rotating* system in the reference angular position:

$$\Delta \mathbf{u}^{(\mathrm{def})}(t) = \mathbf{H}_{\mathrm{P}}\mathbf{q}(t) \tag{2}$$

where $\mathbf{q}(t)$ is the $H \times 1$ vector of modal co-ordinates that are governed by the modal equations of motion:

$$\ddot{\mathbf{q}}(t) + \mathbf{C}\dot{\mathbf{q}}(t) + \mathbf{D}\mathbf{q}(t) = \mathbf{H}_{\mathbf{f}}^{\mathrm{T}}\mathbf{f}(t) \tag{3}$$

and, in Eqs. (2), (3):

- $\mathbf{H}_{\mathrm{P}}$, $\mathbf{H}_{\mathbf{f}}$ are modal transformation matrices whose H columns are mass-normalised eigenvectors corresponding to the undamped natural circular frequencies ϖ_r ($r = 1, \dots, H$) evaluated at the appropriate degrees of freedom.

- The matrices $\mathbf{D}$ and $\mathbf{C}$ are given by

$$\mathbf{D} = \text{diag}([\cdots \varpi_r^2 \cdots]), \quad \mathbf{C} = \text{diag}([\cdots 2\zeta_r \varpi_r \cdots]) \tag{4, 5}$$

where ζ_r is the modal damping ratio. In this work $\mathbf{C}$ is only included to suppress initial transients in the time domain integration for the forced response.

- $\mathbf{f}(t)$ is the $3S \times 1$ vector of external dynamic excitation forces applied to the system (frozen at its reference angular position) at nodes A_s ($s = 1 \ldots S$) in the directions of the Cartesian degrees of freedom there [45].

2.2 Inclusion of Rotation-Induced Inertia Effects

This section describes how the model in section 2.1 is altered to account for rotation-induced inertia effects through the addition of terms to the right hand side of Eq. (3). Fig. 1 shows the coordinate system to be used, which is compatible with the previously described system.
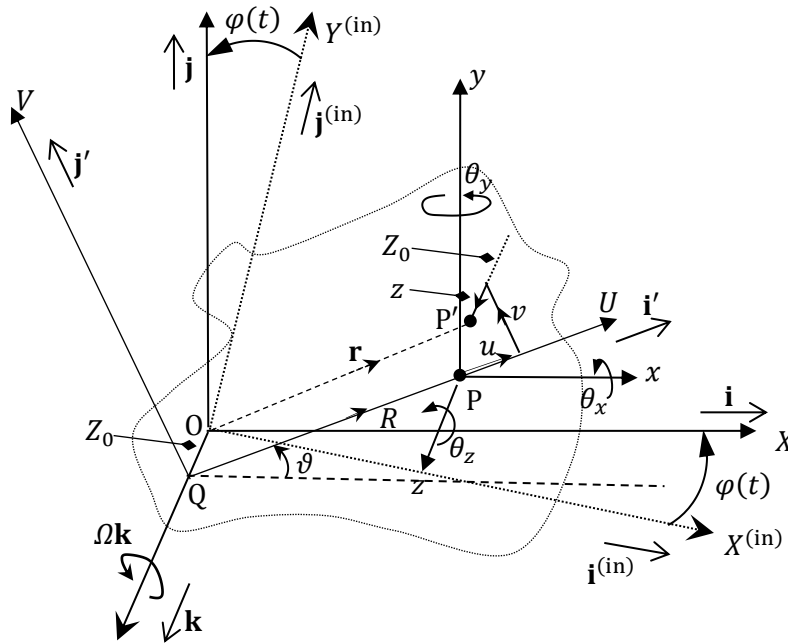

Fig. 1. Rotating structure (inertial axes $OX^{(\text{in})}$, $OY^{(\text{in})}$ are horizontal, vertical respectively)

With reference to Fig. 1,

- axis OZ is completely fixed and along the nominal axis of rotation (independent of tilt);

- the $X^{(in)}$, $Y^{(in)}$ axes through O are inertial, and $\mathbf{i}^{(in)}$, $\mathbf{j}^{(in)}$ are associated unit vectors;

- the X, Y axes through O rotate at the spin velocity $\Omega\mathbf{k}$, where $\Omega = \dot{\varphi}$;

- $\mathbf{i}$, $\mathbf{j}$ are unit vectors associated with X, Y;

- the local Cartesian frame (x, y, z) is always parallel to XYZ;

- the blisk's reference angular position is $\varphi = 0$.

The undeformed position P of an arbitrary point is fixed relative to XYZ and is located within this frame using either Cartesian coordinates (X_0, Y_0, Z_0) or cylindrical coordinates (R, ϑ, Z_0). Axis U coincides with the perpendicular from P to OZ and axis V is normal to both U and Z. Q is the point on the undeformed shaft where the perpendicular from P meets OZ. *It shall be assumed until section 2.5 that the transverse deflection of Q (i.e. the component of its deformation in the plane of rotation UV) is zero.*

The deflection of P to P′ is defined using either the local Cartesian frame (x, y, z) (always parallel to XYZ) or the UVZ frame (u, v, z). Transformation from u, v to x, y and vice-versa is given by

$$\begin{bmatrix} x \\ y \end{bmatrix} = \mathbf{T}(\vartheta) \begin{bmatrix} u \\ v \end{bmatrix}, \quad \begin{bmatrix} u \\ v \end{bmatrix} = \mathbf{T}^{\mathrm{T}}(\vartheta) \begin{bmatrix} x \\ y \end{bmatrix}, \quad \mathbf{T}(\vartheta) = \begin{bmatrix} \cos\vartheta & -\sin\vartheta \\ \sin\vartheta & \cos\vartheta \end{bmatrix} \tag{6a,b,c}$$

In Fig. 1, the angular deformations $\theta_x, \theta_y, \theta_z$ refer to the rotations, about the respective local Cartesian axes, of a vector $\mathbf{n}$ that is attached, and always perpendicular to, a local plane at P, where $\mathbf{n}$ is initially parallel to axis Pz (in case of θ_x, θ_y) or axis Px (in case of θ_z).

As in Eq. (1), rigid rotation is superimposed on the dynamic deformation, and the latter is determined by modal equations with the blisk fixed in the reference angular position. Hence, the transformation to modal coordinates uses the same zero-speed mass-normalised eigenvectors used previously (which neglect rotation-induced inertia effects):

$$\begin{bmatrix} x \\ y \\ z \end{bmatrix} = \begin{bmatrix} \psi_x^{(1)} & \cdots & \psi_x^{(H)} \\ \psi_y^{(1)} & \cdots & \psi_y^{(H)} \\ \psi_z^{(1)} & \cdots & \psi_z^{(H)} \end{bmatrix} \mathbf{q}, \qquad \begin{bmatrix} \theta_x \\ \theta_y \\ \theta_z \end{bmatrix} = \begin{bmatrix} \psi_{\theta_x}^{(1)} & \cdots & \psi_{\theta_x}^{(H)} \\ \psi_{\theta_y}^{(1)} & \cdots & \psi_{\theta_y}^{(H)} \\ \psi_{\theta_z}^{(1)} & \cdots & \psi_{\theta_z}^{(H)} \end{bmatrix} \mathbf{q} \qquad \text{(7a,b)}$$

Using this modal transformation, but accounting for rotational effects, Eq. (3) is updated as follows:

$$\ddot{\mathbf{q}} + \mathbf{C}\dot{\mathbf{q}} + \mathbf{D}\mathbf{q} = \mathbf{H}_{\mathbf{f}}^{\mathrm{T}}\mathbf{f}(t)$$

$$+ \sum_{\mathrm{P}_k} \left\{ \mathbf{H}_{\mathbf{h}_k}^{\mathrm{T}} \left[\mathbf{h}_k(\mathbf{q}, \dot{\mathbf{q}}, \Omega, \dot{\Omega}) + \mathbf{h}_{\mathbf{0}_k}(\Omega, \dot{\Omega}) \right] + \mathbf{H}_{\mathbf{m}_k}^{\mathrm{T}} \mathbf{m}_k(\mathbf{q}, \Omega) + \mathbf{H}_{\mathbf{g}_k}^{\mathrm{T}} \mathbf{g}_k(\dot{\mathbf{q}}, \Omega) \right\} \qquad \text{(8)}$$

In the above approach, the blisk is divided into radial/angular segments (Fig. 2) and the rotational inertia effects from the individual segments, with mass centres at selected FE nodes P_k ($k = 1 \ldots K$), are summed over the entire system and added as additional "external" forces to the modal equation. The nodes P_k are selected from the nodes of the FE mesh used in the non-rotational free undamped vibration analysis (for the mode shapes) so as to coincide as closely as possible with the mass centres of the radial/angular segments in Fig. 2. In Eq. (8):

- $\mathbf{h}_k$ is a 2×1 force vector that contains the Coriolis and spin-softening effects;

- $\mathbf{m}_k$ is a 3×1 moment vector that contains the centrifugal stiffening effect;

- $\mathbf{g}_k$ is a 2×1 moment vector that contains the gyroscopic effect;

- $\mathbf{h}_{\mathbf{0}_k}$ is a 2×1 force vector that is not vibration-dependent, unlike the above vectors.

- $\mathbf{H}_{\mathbf{h}_k}$, $\mathbf{H}_{\mathbf{m}_k}$, $\mathbf{H}_{\mathbf{g}_k}$ are (speed-independent) modal matrices whose H columns are the mass-normalised eigenvectors evaluated at the degrees of freedom associated with $\mathbf{h}_k$, $\mathbf{m}_k$, and $\mathbf{g}_k$ respectively.

Expressions for the vectors $\mathbf{h}_k$, $\mathbf{h}_{\mathbf{0}_k}$, $\mathbf{m}_k$, $\mathbf{g}_k$ are derived in the following subsections.
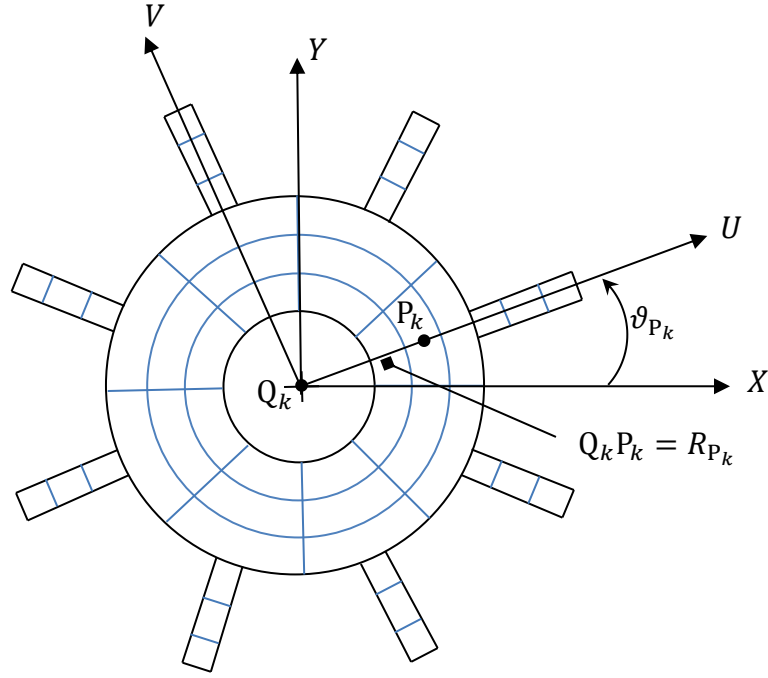
Fig. 2. Blisk radial/angular divisions for rotational inertia effects, where a generic segment has mass centre P_k and mass Δm_{P_k} (same nomenclature as Figure 1 but with P replaced by P_k and Q replaced by Q_k, the shadow point of P_k on axis of rotation).

2.2.1 Coriolis and Spin Softening Effects

With reference to Fig. 1, the position vector of an arbitrary point P′ that was at P prior to deformation is given by

$$\mathbf{r}(t) = \big(R + u(t)\big)\mathbf{i'} + v(t)\mathbf{j'} + \big(Z_0 + z(t)\big)\mathbf{k} \tag{9}$$

where the unit vectors $\mathbf{i'}$, $\mathbf{j'}$ vary with time:

$$\frac{\mathrm{d}}{\mathrm{d}t}(\mathbf{i'}) = \Omega\mathbf{k} \times \mathbf{i'} = \Omega\mathbf{j'} \quad , \quad \frac{\mathrm{d}}{\mathrm{d}t}(\mathbf{j'}) = \Omega\mathbf{k} \times \mathbf{j'} = -\Omega\mathbf{i'} \tag{10a,b}$$

Differentiating Eq. (9) twice with respect to time, and noting Eqs. (10a,b), results in:

$$\ddot{\mathbf{r}} = \ddot{u}\mathbf{i'} + \ddot{v}\mathbf{j'} + \ddot{z}\mathbf{k} - \big[(R + u(t))\Omega^2 + 2\dot{v}\Omega + v(t)\dot{\Omega}\big]\mathbf{i'} + \big[(R + u(t))\dot{\Omega} + 2\dot{u}\Omega - v(t)\Omega^2\big]\mathbf{j'} \tag{11}$$

13

It is evident that the term $\mathbf{h}_k + \mathbf{h}_{0_k}$ in Eq. (8) is the inertial reaction (in Cartesian components) to the rotational acceleration terms in Eq. (11). Hence, applying the transformation Eq. (6a) to the last two terms of Eq. (11), and denoting the mass of the radial/angular segment of P_k as Δm_{P_k}, and relating Fig. 2 to Fig. 1, one obtains

$$\mathbf{h}_k + \mathbf{h}_{0_k} = \Delta m_{P_k} \mathbf{T}(\vartheta_{P_k}) \begin{bmatrix} (R_{P_k} + u_{P_k})\Omega^2 + 2\dot{v}_{P_k}\Omega + v_{P_k}\dot{\Omega} \\ -(R_{P_k} + u_{P_k})\dot{\Omega} - 2\dot{u}_{P_k}\Omega + v_{P_k}\Omega^2 \end{bmatrix} \tag{12}$$

from which

$$\mathbf{h}_{0_k} = \Delta m_{P_k} \mathbf{T}(\vartheta_{P_k}) \begin{bmatrix} R_{P_k}\Omega^2 \\ -R_{P_k}\dot{\Omega} \end{bmatrix} \tag{13}$$

Expressing the u, v terms in Eq. (12) in terms of x, y (using Eq. (6b)), and then the latter to modal coordinates, yields the following expression for $\mathbf{h}_k$:

$$\mathbf{h}_k = \Delta m_{P_k} \mathbf{T}(\vartheta_{P_k}) \left\{ \begin{bmatrix} 0 & 2\Omega \\ -2\Omega & 0 \end{bmatrix} \mathbf{T}^{\mathrm{T}}(\vartheta_{P_k}) \mathbf{H}_{\mathbf{h}_k} \dot{\mathbf{q}} + \begin{bmatrix} \Omega^2 & \dot{\Omega} \\ -\dot{\Omega} & \Omega^2 \end{bmatrix} \mathbf{T}^{\mathrm{T}}(\vartheta_{P_k}) \mathbf{H}_{\mathbf{h}_k} \mathbf{q} \right\} \tag{14}$$

Following Eq. (7a), the matrix $\mathbf{H}_{\mathbf{h}_k}$ (used in Eq. (14) and Eq. (8)) is given by:

$$\mathbf{H}_{\mathbf{h}_k} = \begin{bmatrix} \psi_{x_{P_k}}^{(1)} & \cdots & \psi_{x_{P_k}}^{(H)} \\ \psi_{y_{P_k}}^{(1)} & \cdots & \psi_{y_{P_k}}^{(H)} \\ \psi_{z_{P_k}}^{(1)} & \cdots & \psi_{z_{P_k}}^{(H)} \end{bmatrix} \tag{15}$$
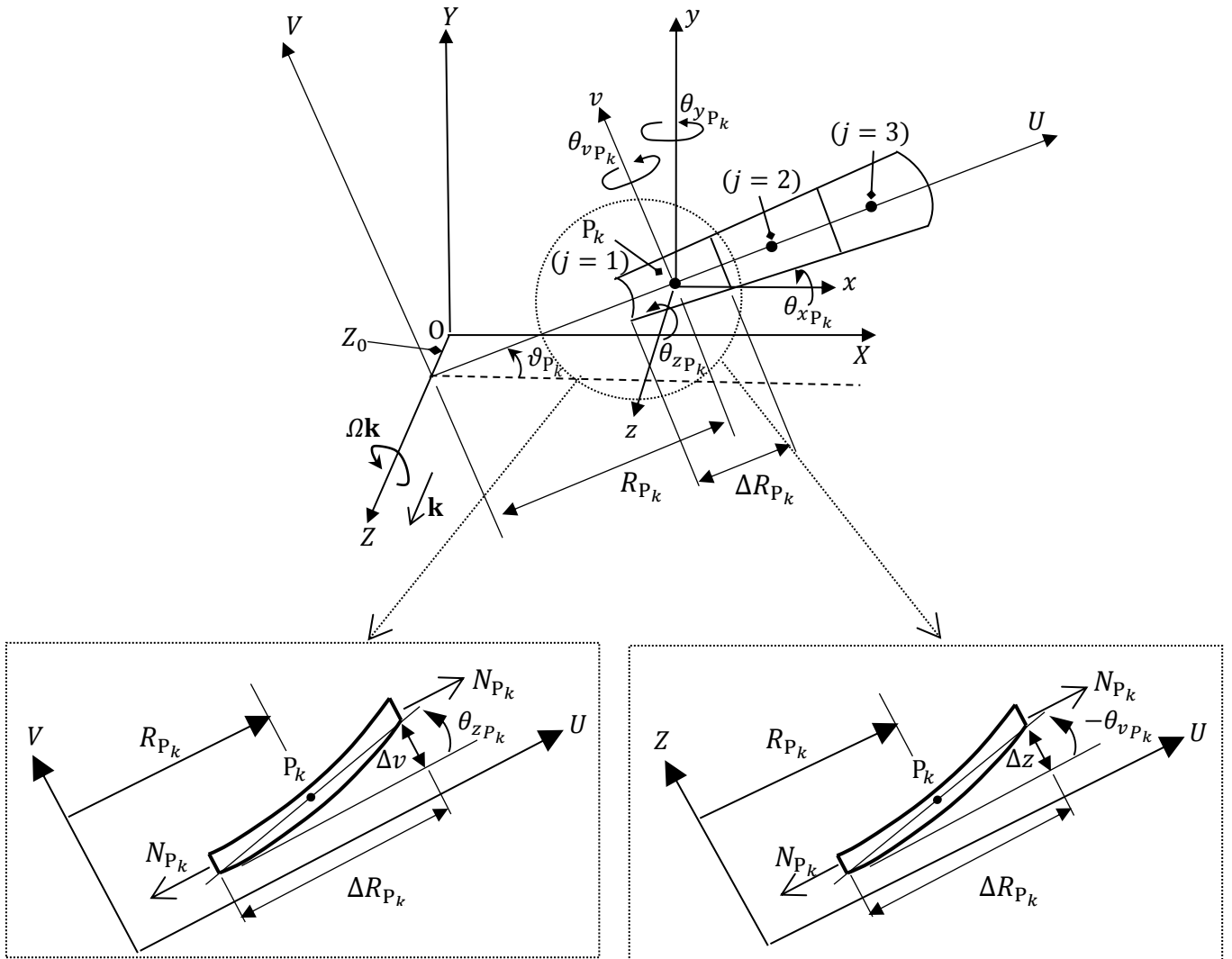
2.2.2 Centrifugal Stiffening

Fig. 3. Modelling of centrifugal stiffening effect

The centrifugal tension N_{P_k} on a radial/angular segment with mass centre P_k $(R_{P_k}, \vartheta_{P_k}, Z_{0_{P_k}})$

of radial extent ΔR_{P_k} (see Fig. 3) is given by:

$$N_{P_k} = \Omega^2 \left\{ \sum_{j=1}^{J} \Delta m_j R_j \right\} \Big|_{R_1 = R_{P_k}} \tag{16}$$

where the summation is applied to radial/angular segments of respective masses Δm_j and radial positions R_j, with mass centres at nodes located along the same angular and axial position of P_k $(\vartheta_{P_k}, Z_{0_{P_k}})$, starting from P_k (i.e. $R_1 = R_{P_k}$) and proceeding radially outward. With reference to Fig. 3, let the deflections v, z increase by Δv, Δz respectively over the radial extent ΔR_{P_k}. The centrifugal tension N_{P_k} stiffens the segment by inducing moments in the edge-wise (UV) and flap-wise (UZ) planes ($M_{z_{P_k}}$, $M_{v_{P_k}}$ respectively) which oppose the corresponding angular deformations $\theta_{z_{P_k}}$, $\theta_{v_{P_k}}$:

$$M_{z_{P_k}} = -N_{P_k}\Delta v = -N_{P_k}\Delta R_{P_k}\frac{\Delta v}{\Delta R_{P_k}} = -N_{P_k}\Delta R_{P_k}\theta_{z_{P_k}} \tag{17}$$

$$M_{v_{P_k}} = N_{P_k}\Delta z = N_{P_k}\Delta R_{P_k}\frac{\Delta z}{\Delta R_{P_k}} = -N_{P_k}\Delta R_{P_k}\theta_{v_{P_k}} \tag{18}$$

Considering Eq. (18) and applying the transformation of Eq. (6a) and then Eq. (6b):

$$\begin{bmatrix} M_{x_{P_k}} \\ M_{y_{P_k}} \end{bmatrix} = M_{v_{P_k}}\begin{bmatrix} -\sin\vartheta_{P_k} \\ \cos\vartheta_{P_k} \end{bmatrix} = -N_{P_k}\Delta R_{P_k}\theta_{v_{P_k}}\begin{bmatrix} -\sin\vartheta_{P_k} \\ \cos\vartheta_{P_k} \end{bmatrix}$$

$$= -N_{P_k}\Delta R_{P_k}\left(-\theta_{x_{P_k}}\sin\vartheta_{P_k} + \theta_{y_{P_k}}\cos\vartheta_{P_k}\right)\begin{bmatrix} -\sin\vartheta_{P_k} \\ \cos\vartheta_{P_k} \end{bmatrix} \tag{19}$$

Hence, combining Eqs. (19) and (17), the centrifugal stiffening moment vector in Eq. (8) is given by:

$$\mathbf{m}_k = -N_{P_k}\Delta R_{P_k}\breve{\mathbf{T}}(\vartheta_{P_k})\begin{bmatrix} \theta_{x_{P_k}} & \theta_{y_{P_k}} & \theta_{z_{P_k}} \end{bmatrix}^{\mathrm{T}} = -N_{P_k}\Delta R_{P_k}\breve{\mathbf{T}}(\vartheta_{P_k})\mathbf{H}_{\mathbf{m}_k}\mathbf{q} \tag{20}$$

Where

$$\breve{\mathbf{T}}\left(\vartheta_{\mathrm{P}_k}\right) = \begin{bmatrix} \sin^2\vartheta_{\mathrm{P}_k} & -\sin\vartheta_{\mathrm{P}_k}\cos\vartheta_{\mathrm{P}_k} & 0 \\ -\sin\vartheta_{\mathrm{P}_k}\cos\vartheta_{\mathrm{P}_k} & \cos^2\vartheta_{\mathrm{P}_k} & 0 \\ 0 & 0 & 1 \end{bmatrix} \tag{21}$$

and, from Eq. (7b):

$$\mathbf{H}_{\mathbf{m}_k} = \begin{bmatrix} \psi_{\theta_{x\mathrm{P}_k}}^{(1)} & \cdots & \psi_{\theta_{x\mathrm{P}_k}}^{(H)} \\ \psi_{\theta_{y\mathrm{P}_k}}^{(1)} & \cdots & \psi_{\theta_{y\mathrm{P}_k}}^{(H)} \\ \psi_{\theta_{z\mathrm{P}_k}}^{(1)} & \cdots & \psi_{\theta_{z\mathrm{P}_k}}^{(H)} \end{bmatrix} \tag{22}$$

2.2.3 Gyroscopic Effects

The angular momentum of a radial/angular segment with mass centre P_k is given by

$$\mathbf{L}_k = \Delta I_{\mathrm{P}_k}\Omega\,\mathbf{n}_k \tag{23}$$

where ΔI_{P_k} is the moment of inertia of the segment about the nominal axis of rotation OZ (Fig. 1) and $\mathbf{n}_k$ is a unit vector that is attached, and always perpendicular to, a local plane at P_k, where $\mathbf{n}_k$ is originally parallel to OZ. Due to deformation, $\mathbf{n}_k$ is given by

$$\mathbf{n}_k = \mathbf{k} + \mathbf{n}_{\mathrm{def}_k}(t) \tag{24}$$

where $\mathbf{n}_{\mathrm{def}_k}(t)$ is the variable part of $\mathbf{n}_k$ due to its change in direction at a precession velocity of $\dot\theta_{x_{P_k}}\mathbf{i} + \dot\theta_{y_{P_k}}\mathbf{j}$.

Hence

$$\dot{\mathbf{L}}_k = \Delta I_{\mathrm{P}_k}\Omega\,\dot{\mathbf{n}}_k = \Delta I_{\mathrm{P}_k}\Omega\left(\dot{\theta}_{x_{P_k}}\mathbf{i} + \dot{\theta}_{y_{P_k}}\mathbf{j}\right)\times\mathbf{n}_k \tag{25}$$

Neglecting second order quantities from Eq. (25) by assuming $\mathbf{i}\times\mathbf{n}_k \approx -\mathbf{j}$ and $\mathbf{j}\times\mathbf{n}_k \approx \mathbf{i}$, one obtains the gyroscopic moment reaction vector $\mathbf{g}_k$ in Eq. (8) as:

$$\mathbf{g}_k = -\dot{\mathbf{L}}_k = \Omega\begin{bmatrix}0 & -\Delta I_{\mathrm{P}_k}\\ \Delta I_{\mathrm{P}_k} & 0\end{bmatrix}\begin{bmatrix}\dot{\theta}_{x_{\mathrm{P}_k}}\\ \dot{\theta}_{y_{\mathrm{P}_k}}\end{bmatrix} = \Omega\begin{bmatrix}0 & -\Delta I_{\mathrm{P}_k}\\ \Delta I_{\mathrm{P}_k} & 0\end{bmatrix}\mathbf{H}_{\mathbf{g}_k}\dot{\mathbf{q}} \tag{26}$$

where, from Eq. (7b):

$$\mathbf{H}_{\mathbf{g}_k} = \begin{bmatrix}\psi^{(1)}_{\theta_{x_{\mathrm{P}_k}}} & \cdots & \psi^{(H)}_{\theta_{x_{\mathrm{P}_k}}}\\ \psi^{(1)}_{\theta_{y_{\mathrm{P}_k}}} & \cdots & \psi^{(H)}_{\theta_{y_{\mathrm{P}_k}}}\end{bmatrix} \tag{27}$$

Notice that, for the simple case where the blisk is rigid and deformation only occurs in the shaft and/or bearings, the time-varying vectors $\mathbf{n}_k$ across the blisk would all be in the same direction at any given instant, which means that the matrices $\mathbf{H}_{\mathbf{g}_k}$ would be identical for all points P_k on the (rigid) blisk.

2.3 Calculation of modal angular displacements

The eigenvectors computed from FE analysis using solid elements express the mode shapes in terms of the Cartesian translational deflections at the nodes i.e. (x, y, z) and do not give angular deformation data i.e. $(\theta_x, \theta_y, \theta_z)$. This section describes how the translational deflections of the mode shape are used to obtain the corresponding angular deformation data required for the matrices of Eqs. (22) and (27).
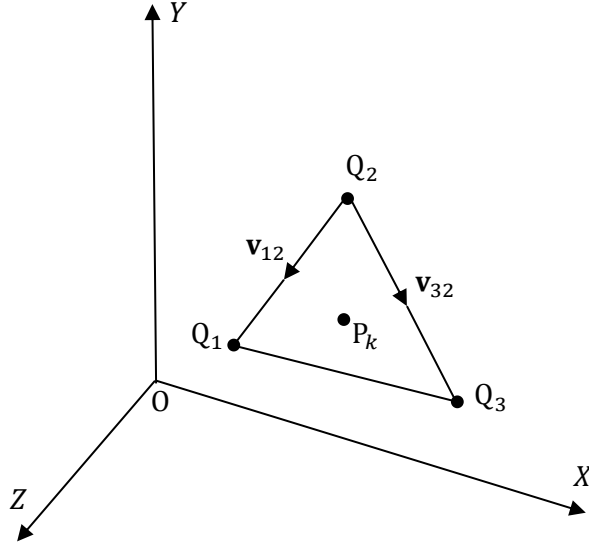
Fig. 4. Local plane through segment mass centre P_k formed by three adjacent nodes

For each FE node corresponding to the centre of mass (P_k) of one of the blisk inertia sectors, three different FE nodes Q_1, Q_2, Q_3 with respective coordinates $\left(X_{0Q_i}, Y_{0Q_i}, Z_{0Q_i}\right)$, $i = 1, 2, 3$, are selected around P_k such that they form a plane parallel to XY plane and containing P_k as shown in Fig. 4. The normal vector $\mathbf{n}$ of the plane is therefore parallel to the Z-axis before deformation. The θ_x, θ_y deformations at P_k corresponding to known translational deformations at Q_i ($x_{Q_i}, y_{Q_i}, z_{Q_i}$) can be determined from the rotation of $\mathbf{n}$ about the y and x axes:

$$\theta_{x_{P_k}} = -\frac{n_y}{n_z} \quad , \quad \theta_{y_{P_k}} = \frac{n_x}{n_z} \tag{28a,b}$$

where

$$\mathbf{n} = n_x \mathbf{i} + n_x \mathbf{j} + n_x \mathbf{k} = \mathbf{v}_{12} \times \mathbf{v}_{32} \tag{29a}$$

$$\mathbf{v}_{12} = \left(X_{Q_1} - X_{Q_2}\right)\mathbf{i} + \left(Y_{Q_1} - Y_{Q_2}\right)\mathbf{j} + \left(Z_{Q_1} - Z_{Q_2}\right)\mathbf{k} \tag{29b}$$

$$\mathbf{v}_{32} = \left(X_{Q_3} - X_{Q_2}\right)\mathbf{i} + \left(Y_{Q_3} - Y_{Q_2}\right)\mathbf{j} + \left(Z_{Q_3} - Z_{Q_2}\right)\mathbf{k} \tag{29c}$$

$$X_{Q_i} = X_{0_{Q_i}} + x_{Q_i}, \quad Y_{Q_i} = Y_{0_{Q_i}} + y_{Q_i}, \quad Z_{Q_i} = Z_{0_{Q_i}} + z_{Q_i} \tag{29d,e,f}$$

The translational and angular deformations at nodes P_k and Q_i in response to a harmonic force $F_{zP_k}(t) = \text{Re}\left\{\tilde{F}_{zP_k} e^{j\omega t}\right\}$ applied at point P_k in the z-direction are given by the following receptance frequency response functions (FRFs):

$$\alpha_{P_k P_k}(\omega) = \frac{\tilde{\theta}_{xP_k}}{\tilde{F}_{zP_k}} = \sum_{r=1}^{H} \frac{A_{P_k P_k}^{(r)}}{\varpi_r^2 - \omega^2} \quad , \quad A_{P_k P_k}^{(r)} = \psi_{\theta_{xP_k}}^{(r)} \psi_{zP_k}^{(r)} \tag{30a,b}$$

$$\beta_{P_k P_k}(\omega) = \frac{\tilde{\theta}_{yP_k}}{\tilde{F}_{zP_k}} = \sum_{r=1}^{H} \frac{B_{P_k P_k}^{(r)}}{\varpi_r^2 - \omega^2} \quad , \quad B_{P_k P_k}^{(r)} = \psi_{\theta_{yP_k}}^{(r)} \psi_{zP_k}^{(r)} \tag{31a,b}$$

$$\gamma_{Q_i P_k}(\omega) = \frac{\tilde{x}_{Q_i}}{\tilde{F}_{zP_k}} = \sum_{r=1}^{H} \frac{C_{Q_i P_k}^{(r)}}{\varpi_r^2 - \omega^2} \quad , \quad C_{Q_i P_k}^{(r)} = \psi_{xQ_i}^{(r)} \psi_{zP_k}^{(r)} \tag{32a,b}$$

$$\sigma_{Q_i P_k}(\omega) = \frac{\tilde{y}_{Q_i}}{\tilde{F}_{zP_k}} = \sum_{r=1}^{H} \frac{D_{Q_i P_k}^{(r)}}{\varpi_r^2 - \omega^2} \quad , \quad D_{Q_i P_k}^{(r)} = \psi_{yQ_i}^{(r)} \psi_{zP_k}^{(r)} \tag{33a,b}$$

$$\varepsilon_{Q_i P_k}(\omega) = \frac{\tilde{z}_{Q_i}}{\tilde{F}_{zP_k}} = \sum_{r=1}^{H} \frac{E_{Q_i P_k}^{(r)}}{\varpi_r^2 - \omega^2} \quad , \quad E_{Q_i P_k}^{(r)} = \psi_{zQ_i}^{(r)} \psi_{zP_k}^{(r)} \tag{34a,b}$$

where:

- $x_{P_k}(t) = \text{Re}\left\{\tilde{x}_{P_k} e^{j\omega t}\right\}$, ...etc, $\theta_{xP_k}(t) = \text{Re}\left\{\tilde{\theta}_{xP_k} e^{j\omega t}\right\}$,...etc;

- $x_{Q_i}(t) = \text{Re}\left\{\tilde{x}_{Q_i} e^{j\omega t}\right\}$, ...etc, $(i = 1,2.3)$;

- $\varpi_r, r = 1 \dots H$, are the undamped natural circular frequencies.

The only unknowns in Eqs. (30-34) are the modal angular deformations $\psi_{\theta_{xP_k}}^{(r)}, \psi_{\theta_{yP_k}}^{(r)}$, all other modal displacements being translational and output from FE analysis. The values of $\psi_{\theta_{xP_k}}^{(r)}, \psi_{\theta_{yP_k}}^{(r)}$ are determined as follows.

1. Set $\widetilde{F}_{z_{P_k}} = 1$.

2. For a given excitation frequency ω, calculate the amplitudes $\tilde{x}_{Q_i}, \tilde{y}_{Q_i}, \tilde{z}_{Q_i}$ $(i = 1,2.3)$ from Eqs. (32-34).

3. Determine the corresponding amplitudes $\tilde{\theta}_{x_{P_k}}$, $\tilde{\theta}_{y_{P_k}}$ (and hence the FRFs $\alpha_{P_k P_k}(\omega)$, $\beta_{P_k P_k}(\omega)$ on the left hand sides of Eqs. (30a), (31a)) using Eqs. (28) and (29) with $x_{Q_i}, y_{Q_i}, z_{Q_i}$ replaced by $\tilde{x}_{Q_i}, \tilde{y}_{Q_i}, \tilde{z}_{Q_i}$.

4. Repeat steps 1-3 for excitation frequencies $\omega = \omega_n$, $n = 1 \dots N$ $(N > H)$ thus determining the FRF values $\alpha_{P_k P_k}(\omega_n), \beta_{P_k P_k}(\omega_n)$ on the left hand sides of Eqs. (30a), (31a).

5. Determine $A_{P_k P_k}^{(r)}$ on the right hand side of Eq. (30a) by solving the least-squares problem:

$$
\begin{bmatrix} \alpha_{P_k P_k}(\omega_1) \\ \alpha_{P_k P_k}(\omega_2) \\ \vdots \\ \alpha_{P_k P_k}(\omega_N) \end{bmatrix}_{N \times 1} = \begin{bmatrix} \dfrac{1}{\varpi_1^2 - \omega_1^2} & \dfrac{1}{\varpi_2^2 - \omega_1^2} & \cdots & \dfrac{1}{\varpi_H^2 - \omega_1^2} \\ \dfrac{1}{\varpi_1^2 - \omega_2^2} & \dfrac{1}{\varpi_2^2 - \omega_2^2} & \cdots & \dfrac{1}{\varpi_H^2 - \omega_2^2} \\ \vdots & \vdots & \cdots & \vdots \\ \dfrac{1}{\varpi_1^2 - \omega_N^2} & \dfrac{1}{\varpi_2^2 - \omega_N^2} & \cdots & \dfrac{1}{\varpi_H^2 - \omega_N^2} \end{bmatrix}_{N \times H} \begin{bmatrix} A_{P_k P_k}^{(1)} \\ A_{P_k P_k}^{(2)} \\ \vdots \\ A_{P_k P_k}^{(H)} \end{bmatrix}_{H \times 1} \tag{35}
$$

6. From Eq. (30b), determine $\psi_{\theta_{x_{P_k}}}^{(r)}$.

7. Determine $\psi_{\theta_{y_{P_k}}}^{(r)}$ by repeating steps 5-6 for $B_{P_k P_k}^{(r)}$ using Eqs. (31a) and (31b).

A similar procedure is followed to obtain the modal angular deformations $\psi_{\theta_{z_{P_k}}}^{(r)}$, with the following modifications:

- The nodes Q_1, Q_2, Q_3 are chosen to lie in a plane which is parallel to the YZ plane.

- Equations (30), (31) are replaced by the FRF relating $\widetilde{F}_{x_{P_k}}$ with $\theta_{z_{P_k}}$, and Eqs. (32-34) modified by replacing subscript "z_{P_k}" with "x_{P_k}".

- Replace Eq. (28) with the following formula:

$$\theta_{z_{P_k}} = \frac{n_y}{n_x} \tag{36}$$

2.4 Campbell Diagrams and Forced Response

Substituting, Eqs. (13), (14), (20), and (26) into Eq. (8), results in the following modal equation:

$$\ddot{\mathbf{q}} + \{\mathbf{C} + \Omega(\mathbf{G} + \mathbf{A}_1)\}\dot{\mathbf{q}} + \{\mathbf{D} + \Omega^2(\mathbf{N} + \mathbf{A}_2) + \dot{\Omega}\mathbf{A}_3\}\mathbf{q} = \mathbf{H}_{\mathbf{f}}^{\mathrm{T}}\mathbf{f}(t) + \mathbf{a}_0(\Omega^2, \dot{\Omega}) \tag{37}$$

where the speed-independent matrices $\mathbf{G}$, $\mathbf{A}_1$, $\mathbf{N}$, $\mathbf{A}_2$, $\mathbf{A}_3$ respectively contain the gyroscopic, Coriolis, centrifugal stiffening, spin-softening and angular acceleration effects. These matrices, along with the speed-dependent vector $\mathbf{a}_0$ are given by the following expressions.

$$\mathbf{G} = \sum_{P_k} \left\{ \Delta I_{P_k} \mathbf{H}_{\mathbf{g}_k}^{\mathrm{T}} \begin{bmatrix} 0 & 1 \\ -1 & 0 \end{bmatrix} \mathbf{H}_{\mathbf{g}_k} \right\} \tag{38}$$

$$\mathbf{A}_1 = -2 \sum_{P_k} \left\{ \Delta m_{P_k} \mathbf{H}_{\mathbf{h}_k}^{\mathrm{T}} \mathbf{T}(\vartheta_{P_k}) \begin{bmatrix} 0 & 1 \\ -1 & 0 \end{bmatrix} \mathbf{T}^{\mathrm{T}}(\vartheta_{P_k}) \mathbf{H}_{\mathbf{h}_k} \right\} \tag{39}$$

$$\mathbf{N} = \sum_{P_k} \left\{ \Delta R_{P_k} \widehat{N}_{P_k} \mathbf{H}_{\mathbf{m}_k}^{\mathrm{T}} \breve{\mathbf{T}}(\vartheta_{P_k}) \mathbf{H}_{\mathbf{m}_k} \right\} \quad , \quad \widehat{N}_{P_k} = \left\{ \sum_{j=1}^{J} \Delta m_j R_j \right\} \bigg|_{R_1 = R_{P_k}} \tag{40a,b}$$

$$\mathbf{A}_2 = -\sum_{\mathrm{P}_k} \left\{ \Delta m_{\mathrm{P}_k} \mathbf{H}_{\mathbf{h}_k}^{\mathrm{T}} \mathbf{T}(\vartheta_{\mathrm{P}_k}) \begin{bmatrix} 1 & 0 \\ 0 & 1 \end{bmatrix} \mathbf{T}^{\mathrm{T}}(\vartheta_{\mathrm{P}_k}) \mathbf{H}_{\mathbf{h}_k} \right\} \tag{41}$$

$$\mathbf{A}_3 = -\sum_{\mathrm{P}_k} \left\{ \Delta m_{\mathrm{P}_k} \mathbf{H}_{\mathbf{h}_k}^{\mathrm{T}} \mathbf{T}(\vartheta_{\mathrm{P}_k}) \begin{bmatrix} 0 & 1 \\ -1 & 0 \end{bmatrix} \mathbf{T}^{\mathrm{T}}(\vartheta_{\mathrm{P}_k}) \mathbf{H}_{\mathbf{h}_k} \right\} \tag{42}$$

$$\mathbf{a}_0(\Omega^2, \dot{\Omega}) = \sum_{\mathrm{P}_k} \left\{ \Delta m_{\mathrm{P}_k} \mathbf{H}_{\mathbf{h}_k}^{\mathrm{T}} \mathbf{T}(\vartheta_{\mathrm{P}_k}) \begin{bmatrix} R_{\mathrm{P}_k} \Omega^2 \\ -R_{\mathrm{P}_k} \dot{\Omega} \end{bmatrix} \right\} \tag{43}$$

2.4.1 Campbell Diagrams

The undamped natural frequencies and mode shapes at a given speed are found by setting $\dot{\Omega} = 0$ and solving the eigenvalue problem associated with the homogeneous form of Eq. (37):

$$\ddot{\mathbf{q}} + \{\mathbf{C} + \Omega(\mathbf{G} + \mathbf{A}_1)\}\dot{\mathbf{q}} + \{\mathbf{D} + \Omega^2(\mathbf{N} + \mathbf{A}_2)\}\mathbf{q} = \mathbf{0} \tag{44}$$

In order to solve the eigenproblem, the state space format of Eq. (44) is used:

$$\begin{bmatrix} \mathbf{I}_H & \mathbf{0} \\ \mathbf{0} & \mathbf{I}_H \end{bmatrix} \frac{\mathrm{d}}{\mathrm{d}t} \begin{bmatrix} \mathbf{q}^{\mathrm{T}} \\ \dot{\mathbf{q}}^{\mathrm{T}} \end{bmatrix} + \begin{bmatrix} \mathbf{0} & -\mathbf{I}_H \\ \{\mathbf{D} + \Omega^2(\mathbf{N} + \mathbf{A}_2)\} & \{\mathbf{C} + \Omega(\mathbf{G} + \mathbf{A}_1)\} \end{bmatrix} \begin{bmatrix} \mathbf{q}^{\mathrm{T}} \\ \dot{\mathbf{q}}^{\mathrm{T}} \end{bmatrix} = \mathbf{0} \tag{45}$$

or $\quad \mathbf{I}_{2H}\dot{\mathbf{s}} + \mathbf{B}\mathbf{s} = \mathbf{0}$

where the state vector $\mathbf{s} = [\mathbf{q}^{\mathrm{T}} \quad \dot{\mathbf{q}}^{\mathrm{T}}]^{\mathrm{T}}$ and $\mathbf{I}_H$ is an H-square identity matrix.

Let $\quad \mathbf{s} = \mathbf{c}e^{\lambda t}$ and substituting in Eq. (45):

$$(\lambda \mathbf{I}_{2H} + \mathbf{B})\mathbf{c} = \mathbf{0} \tag{46}$$

The above eigenvalue problem is solved for a given speed using the *eig.m* function in Matlab [42]. Using a range of speeds, the natural frequencies are calculated at each speed (from the imaginary part of the eigenvalues λ) and the Campbell diagram is plotted.

2.4.2 Forced Response

The system in Eq. (37) is cast in state-space format

$$\dot{\mathbf{s}} = \boldsymbol{\chi}(\mathbf{s}, t) \tag{47a}$$

where $\mathbf{s} = [\mathbf{q}^{\mathrm{T}} \quad \dot{\mathbf{q}}^{\mathrm{T}}]^{\mathrm{T}}$ and the vector function $\boldsymbol{\chi}$ is

$$\boldsymbol{\chi} = \begin{bmatrix} \mathbf{0} & \mathbf{I}_H \\ -\{\mathbf{D} + \Omega^2(\mathbf{N} + \mathbf{A}_2) + \dot{\Omega}\mathbf{A}_3\} & -\{\mathbf{C} + \Omega(\mathbf{G} + \mathbf{A}_1)\} \end{bmatrix} \mathbf{s} + \mathbf{H}_{\mathrm{f}}^{\mathrm{T}}\mathbf{f}(t) + \mathbf{a}_0(\Omega^2, \dot{\Omega}) \tag{47b}$$

The time domain response to a prescribed excitation $\mathbf{f}(t)$ (e.g. travelling wave chirp signal [42]), under arbitrary time-varying speed condition $\Omega(t)$, is then found by solving Eq. (47) using any one of the numerical integration routines in the *ode* suite of Matlab [46]. The dynamic response in the rotating *XYZ* frame (Fig. 1) is then given by Eq. (2) i.e. $\Delta\mathbf{u}^{(\mathrm{def})}$. From this, the absolute coordinates of any subset of FE nodes can be determined using Eq. (1). For use in the BTT simulator of [42,45], Eq. (47) is solved in Simulink and used in conjunction with Eqs. (1), (2), and the *Hit Crossing* block, to determine the blade tip timing values (as done previously with the state-space form of Eq. (3) [42]).

2.5 Inclusion of Shaft Deflection – Extension to Shaft-Blisk System

The effect of the deflection of point Q in Figure 1 is now considered. Let Q move to a point Q′. The position vector of the deformed position P′ of P (Eq. (9)) is now rewritten as:

$$\mathbf{r}(t) = X_{Q'}^{(in)}(t)\mathbf{i}^{(in)} + Y_{Q'}^{(in)}(t)\mathbf{j}^{(in)} + \left(R + u(t) - u_{Q'}(t)\right)\mathbf{i}' + \left(v(t) - v_{Q'}(t)\right)\mathbf{j}' \tag{48}$$
$$+ \left(Z_0 + z(t)\right)\mathbf{k}$$

where

$$X_{Q'}^{(in)}(t)\mathbf{i}^{(in)} + Y_{Q'}^{(in)}(t)\mathbf{j}^{(in)} \equiv u_{Q'}(t)\mathbf{i}' + v_{Q'}(t)\mathbf{j}'$$

is the transverse component of the position vector of Q′, and hence the transverse deflection
of Q. The position vector $\mathbf{r}(t)$ of P′ in Eq. (48) can be written as

$$\mathbf{r}(t) = X^{(in)}(t)\mathbf{i}^{(in)} + Y^{(in)}(t)\mathbf{j}^{(in)} + \left(Z_0 + z(t)\right)\mathbf{k} \tag{49}$$

where the absolute coordinates $X^{(in)}(t)$, $Y^{(in)}(t)$ of the deformed position of P, P′ are

$$\begin{bmatrix} X^{(in)}(t) \\ Y^{(in)}(t) \end{bmatrix} = \begin{bmatrix} X_{Q'}^{(in)}(t) \\ Y_{Q'}^{(in)}(t) \end{bmatrix} + \mathbf{T}(\varphi(t)) \begin{bmatrix} R\cos\vartheta \\ R\sin\vartheta \end{bmatrix} + \mathbf{T}(\varphi(t)) \begin{bmatrix} x(t) - x_{Q'}(t) \\ y(t) - y_{Q'}(t) \end{bmatrix} \tag{50}$$

The modal matrices of the shaft-blisk system at zero-speed are used for transformation to the
modal coordinate vector $\mathbf{q}(t)$:

$$\begin{bmatrix} X_{Q'}^{(in)}(t) \\ Y_{Q'}^{(in)}(t) \end{bmatrix} = \begin{bmatrix} \psi_{x_Q}^{(1)} & \cdots & \psi_{x_Q}^{(H)} \\ \psi_{y_Q}^{(1)} & \cdots & \psi_{y_Q}^{(H)} \end{bmatrix} \mathbf{q}(t) \tag{51}$$

$$\begin{bmatrix} x(t) - x_{Q'}(t) \\ y(t) - y_{Q'}(t) \end{bmatrix} = \left\{ \begin{bmatrix} \psi_x^{(1)} & \cdots & \psi_x^{(H)} \\ \psi_y^{(1)} & \cdots & \psi_y^{(H)} \end{bmatrix} - \begin{bmatrix} \psi_{x_Q}^{(1)} & \cdots & \psi_{x_Q}^{(H)} \\ \psi_{y_Q}^{(1)} & \cdots & \psi_{y_Q}^{(H)} \end{bmatrix} \right\} \mathbf{q}(t) \tag{52}$$

In Eq. (50), the transformation matrix $\mathbf{T}$ is defined in Eq. (6c) and $\varphi(t)$ is the rigid rotation.

Hence, the simulator equation (1) is extended to a shaft-blisk system as follows

$$\Delta \mathbf{u}^{(\text{def})}(t) = \mathbf{T}_{\text{aug}}^{-1}(\varphi(t))\mathbf{H}_{\text{Q}}\mathbf{q}(t) + (\mathbf{H}_{\text{P}} - \mathbf{H}_{\text{Q}})\mathbf{q}(t) \tag{53}$$

$\mathbf{H}_{\text{P}}$, as before, is the modal matrix for points on the blisk, and $\mathbf{H}_{\text{Q}}$ the modal matrix of their companion points on the shaft centreline (as per Figure 1), both matrices evaluated from modal analysis of the system at zero speed with the blisk in its reference angular position.

The above equations mean that the following two modifications A, B to the analysis of the previous sections are necessary to extend it shaft-blisk systems.

A. The expression for $\mathbf{H}_{\mathbf{h}_k}$ in Eq. (15) is replaced by the following

$$\mathbf{H}_{\mathbf{h}_k} = \begin{bmatrix} \psi_{x_{\text{P}_k}}^{(1)} & \cdots & \psi_{x_{\text{P}_k}}^{(H)} \\ \psi_{y_{\text{P}_k}}^{(1)} & \cdots & \psi_{y_{\text{P}_k}}^{(H)} \end{bmatrix} - \begin{bmatrix} \psi_{x_{\text{Q}_k}}^{(1)} & \cdots & \psi_{x_{\text{Q}_k}}^{(H)} \\ \psi_{y_{\text{Q}_k}}^{(1)} & \cdots & \psi_{y_{\text{Q}_k}}^{(H)} \end{bmatrix} \tag{54}$$

where Q_k is the shaft centreline counterpart to point P_k on the blisk (see Figure 2; note that there will be multiple points Q_k all coinciding with the same point on the shaft centreline, as many as there are points P_k in a given plane normal to shaft centreline).

B. A modal parametric excitation term $\boldsymbol{\rho}$ is added to Eqs. (8) and (37):

$$\boldsymbol{\rho}(\varphi(t), \mathbf{q}, \dot{\mathbf{q}}, \ddot{\mathbf{q}}, \Omega, \dot{\Omega}) =$$

$$\Delta \mathbf{M}(\varphi(t))\ddot{\mathbf{q}} + \Omega \cdot \Delta \mathbf{A}_1(\varphi(t))\dot{\mathbf{q}} + \Omega^2 \cdot \Delta \mathbf{A}_2(\varphi(t))\mathbf{q} + \dot{\Omega} \cdot \Delta \mathbf{A}_3(\varphi(t))\mathbf{q} + \Delta \mathbf{a}_0(\varphi(t), \Omega^2, \Omega) \tag{55}$$

where $\Delta \mathbf{M}, \Delta \mathbf{A}_1, \Delta \mathbf{A}_2, \Delta \mathbf{A}_3, \Delta \mathbf{a}_0$ are time-varying matrices.

Modification A is evident by comparing the last three terms in Eq. (48) to Eq. (9). Modification B is the result of the first term in Eq. (48), which means that the system now has

a deformable part that does not rotate (this part is defined by the collective of points Q originally along OZ in Figure 1).

Adding Eq. (55) to Eq. (37), results in the following equations of motion for the shaft-blisk system:

$$\ddot{\mathbf{q}} + \{\mathbf{C} + \Omega(\mathbf{G} + \mathbf{A}_1)\}\dot{\mathbf{q}} + \left\{\mathbf{D} + \Omega^2(\mathbf{N} + \mathbf{A}_2) + \dot{\Omega}\mathbf{A}_3\right\}\mathbf{q} \tag{56}$$
$$= \mathbf{H}_f^{\mathrm{T}}\mathbf{f}(t) + \mathbf{a}_0\left(\Omega^2, \dot{\Omega}\right) + \boldsymbol{\rho}\left(\varphi(t), \mathbf{q}, \dot{\mathbf{q}}, \ddot{\mathbf{q}}, \Omega, \dot{\Omega}\right)$$

where all modal parameters belong to the shaft-blisk system at zero speed. In other works on shaft-blisk systems e.g. Santos et al. [44], the first four terms of $\boldsymbol{\rho}$ in Eq. (55) are incorporated with the corresponding terms on the left hand side of the equations of motion, rather than collected on the right hand side as above. The derivation of expressions for the terms of $\boldsymbol{\rho}$ is outside the scope of this paper.

$\boldsymbol{\rho}$ is only zero for $\varphi, \Omega, \dot{\Omega} = 0$. For Ω constant (i.e. $\dot{\Omega} = 0$), $\boldsymbol{\rho}$ is periodic and introduces parametric excitation into the system. In this condition, the coefficients of $\mathbf{q}, \dot{\mathbf{q}}, \ddot{\mathbf{q}}$ in Eq. (56) are not constant matrices and eigenvalue analysis for the Campbell diagrams cannot be performed since this requires constant matrices. However, in this paper, the parametric excitation effect is not considered. Hence, the eigenvalue analysis for Campbell diagrams for the rotor-blisk system is performed at any fixed speed Ω as before (section 2.4.1), with modification A (above) but with the parametric term $\boldsymbol{\rho}$ omitted. The same thing was done by Ma et al. [2] and Chun and Lee [18], who did eigenvalue analysis of the rotor-blisk system equations but did not declare the omission of any periodically varying terms in the matrices (in fact, there is no mention of parametric excitation in these papers). The Campbell diagrams so generated in these references [2,18] are indeed verified by the present analysis

(sections 3.4.2 and 3.5). Forced vibration analysis is done as in section 2.4.2 merely to cross-check the resulting resonances with the results of the Campbell diagram.

If $\boldsymbol{\rho}$ is *not* omitted, rather than generating Campbell diagrams via eigenvalue analysis, one generates waterfall diagrams (WDs) by integrating for the time domain responses of Eq. (56) over a range of fixed speeds Ω and then taking their Fast Fourier Transforms (FFTs), as done by Santos et al. [44]. The researchers [44] considered a simple model of a rotor-blades assembly, where the rotor was mounted with lateral flexibility to simulate shaft deflection. The external excitation consisted of a rotating unbalance (via term $\Delta \mathbf{a}_0$ in Eq. (55)) and impulses applied to either a blade or the rotor. The WDs all contained frequencies Ω. The WDs of the rotor lateral vibration (in an inertial coordinate frame, Figures 5, 7 in reference [44]) additionally showed frequencies of the form $\omega_n \pm \Omega$, where ω_n is one of the natural frequencies of the shaft-blades system at zero speed. Such *parametric vibration frequencies* were not evident in the WDs of the blades response (in a rotating coordinate frame, Figures 6, 8 in reference [44]), which showed variation in one of the natural frequencies that appears to be similar to the variation on a Campbell diagram obtained as discussed above (i.e. excluding $\boldsymbol{\rho}$). This justifies, to a certain extent, the approach taken in this paper, as well as in references [2, 18]. It should be noted that the researchers [44] also considered gravitational forces, as well as nonlinearity (which are not considered here).

3. VALIDATION

This section presents a number of examples of shaft-disk-blades assemblies considering one or more of the rotational effects. All assemblies are modelled and analysed using the method presented in the previous section, and the results are correlated against analytical or experimental results from the literature, or results from commercial FE software.

The examples considered are presented in Table 1. Example #0 is not actually about rotational effects, but about the effective stiffness variation induced by a longitudinal load on a beam. It therefore serves as a preliminary verification of the accuracy of the original approach introduced in section 2.2.2 for considering the centrifugal stiffening effect. For examples #3a, #3b and #4, which are shaft-blisk systems, the parametric excitation effect is omitted, as per last two paragraphs of section 2.5.

Table 1: Examples used for model validation

Example	Effects considered	Validation Source
0	Longitudinal load on beam (preliminary check for Example 1)	Shaker, 1975 [47]
1	Centrifugal Stiffening	Chen et al., 2016 [39]
2	Coriolis forces	Ruffini et al, 2015 [32]
3a	Gyroscopic moment – effect of disk flexibility	*ANSYS* FE software
3b	Gyroscopic moment – example from literature	Chun and Lee, 1996 [18]/ Zhang et al, 1994 [48]
4	Gyroscopic, Coriolis, Spin Softening, Centrifugal Stiffening	Ma et al, 2015 [2]

3.1 Example # 0 – Longitudinal Load on Beam (Table 1, preliminary check for section 2.2.2)

Fig. 5 shows a rectangular-section cantilever beam ($b = 5h$) subjected to a constant longitudinal force. Using an analytical approach, Shaker [47] calculated the natural frequencies of the beam for a range of force values (tension and compression).
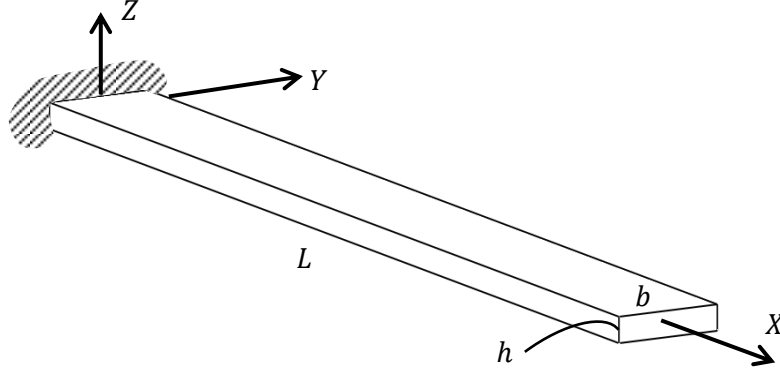
Fig. 5. Example 0 - Cantilever beam subjected to axial load

With the proposed method, for an applied load of Q ($Q > 0$ for compression), Eqs. (44) and (40a,b) are modified as follows:

$$\ddot{\mathbf{q}} + \{\mathbf{D} + \mathbf{N}_{\text{mod}}\}\mathbf{q} = \mathbf{0} \tag{57}$$

$$\mathbf{N}_{\text{mod}} = \sum_{\mathrm{P}_k} \left\{ \Delta R_{\mathrm{P}_k} \ \widehat{N}_{\mathrm{P}_{k\text{mod}}} \mathbf{H}_{\mathbf{m}_k}^{\mathrm{T}} \breve{\mathbf{T}}(\vartheta_{\mathrm{P}_k}) \mathbf{H}_{\mathbf{m}_k} \right\} \quad , \quad \widehat{N}_{\mathrm{P}_{k\text{mod}}} = -Q \tag{58a,b}$$

It is seen from Eqs. (58a,b) that Eqs. (40a,b) were modified to allow for a compressive load that is constant for all segments (and not varying as in centrifugal forces). 200 divisions (points P_k) were used for accuracy. From Fig. 5 and Fig. 3, $\vartheta_{\mathrm{P}_k} = 0$ in Eq. (21). The basis modes used in the matrices $\mathbf{D}$ and $\mathbf{H}_{\mathbf{m}_k}$ pertain to the undamped modes of the given cantilever at zero longitudinal load. The number of basis modes $= 10$ i.e. 5 modes were used for each bending plane *XZ* and *XY*. The basis modes in each plane were calculated using exact formulas for natural circular frequencies and mass normalized mode shapes of the cantilever at zero longitudinal load (found in [49]), such that Eqs. (4), (5) are given by

$$\mathbf{D} = \text{diag}([\varpi_{YY_1} \quad \varpi_{ZZ_1} \quad \varpi_{YY_2} \quad \varpi_{ZZ_2} \quad \cdots\cdots]) \tag{59}$$

$$\mathbf{H_{m_k}} = \begin{bmatrix} 0 & 0 & 0 & 0 & \cdots\cdots \\ -\dfrac{\mathrm{d}\phi_Z^{(1)}}{\mathrm{d}X} & 0 & -\dfrac{\mathrm{d}\phi_Z^{(2)}}{\mathrm{d}X} & 0 & \cdots\cdots \\ 0 & \dfrac{\mathrm{d}\phi_Y^{(1)}}{\mathrm{d}X} & 0 & \dfrac{\mathrm{d}\phi_Y^{(2)}}{\mathrm{d}X} & \cdots\cdots \end{bmatrix} \tag{60}$$

where ϖ_{YY_i}, $\phi_Z^{(i)}$ denote the natural circular frequency and translational mode shape for i^{th} bending mode of the cantilever in the XZ plane (i.e. bending about YY neutral axis) at zero longitudinal load, and ϖ_{ZZ_i}, $\phi_Y^{(i)}$ denote similar quantities for the XY plane.
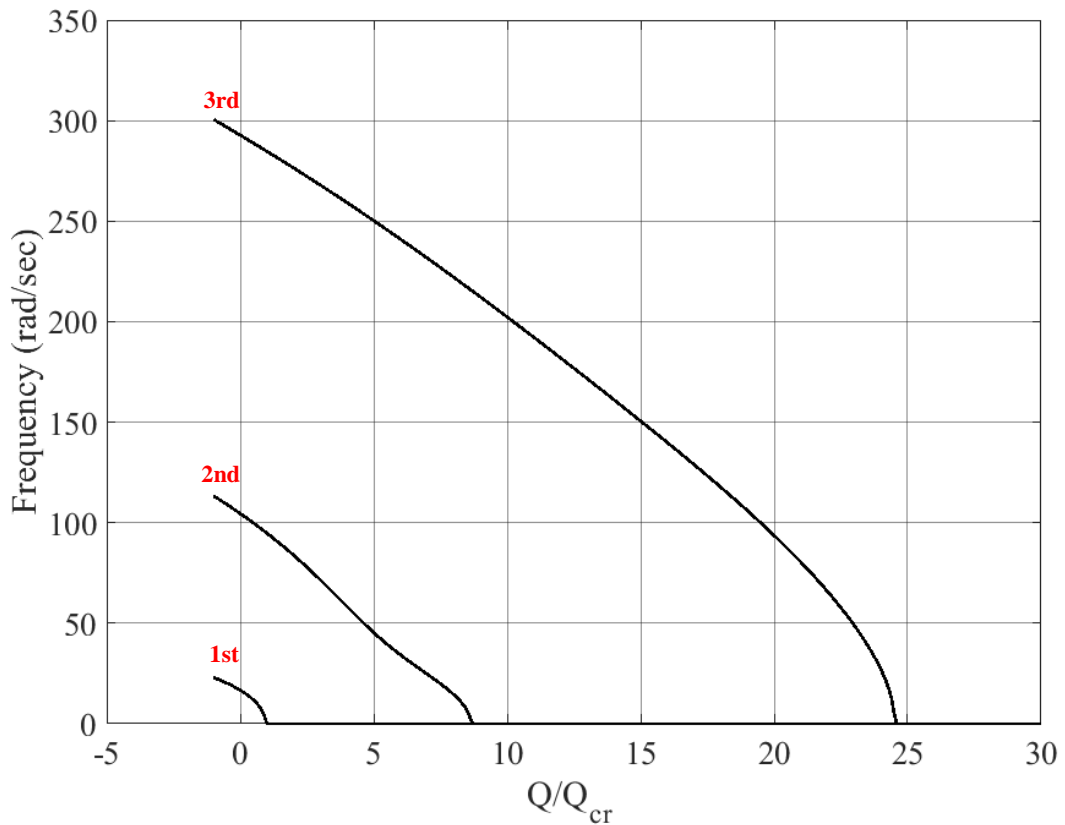
Fig. 6. Example 0 - natural frequencies vs axial load ($XZ-$ plane)
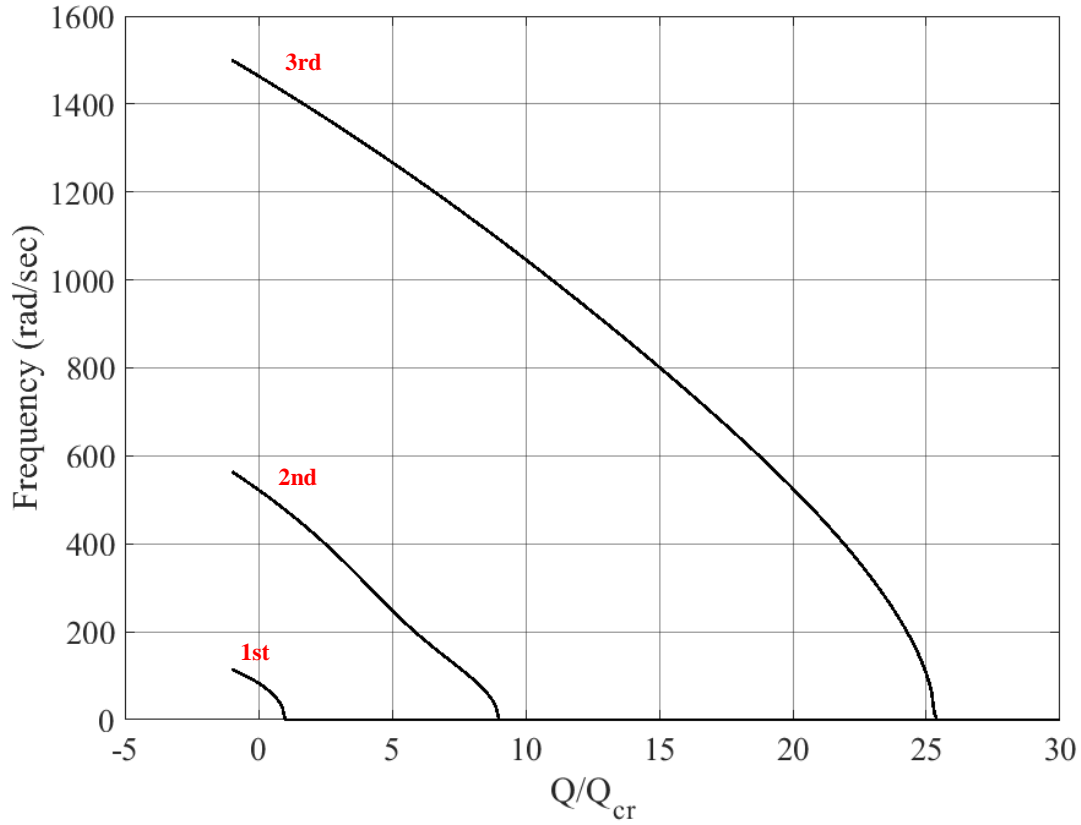
Fig. 7. Example 0 - natural frequencies vs axial load ($XY-$ plane)

The eigenvalue problem defined by Eq. (57) was then solved for each given value of Q within a wide range. The eigenvalue problem yields natural frequencies for bending in each plane XZ, XY. Fig. 6 shows the variation of the first three natural frequencies for bending in the XZ plane with $Q/Q_{cr_{YY}}$ and Fig. 7 shows the variation of the first three natural frequencies for bending in the XY plane with $Q/Q_{cr_{ZZ}}$ and where $Q_{cr_{YY}}$, $Q_{cr_{ZZ}}$ respectively denote the first critical buckling loads of the cantilever in the XZ, XY planes:

$$Q_{cr_{YY,ZZ}} = \frac{\pi^2 EI_{YY,ZZ}}{(2L)^2} \tag{61}$$

where L is the length and EI_{YY}, EI_{ZZ} denote the flexural rigidity in the XZ, XY planes respectively. As per theory in [50], for either plane, the first natural frequency goes to zero when $Q/Q_{cr} = 1$ (first critical buckling load), while the second one becomes zero at

32

$Q/Q_{cr} = 9$ (second critical buckling load), and the third frequency goes to zero at $Q/Q_{cr} = 25$ (third critical buckling load). Fig. 8 shows the variation of the non-dimensional natural frequency λ_i^2 in XZ plane ($\lambda_i^2 = \omega_{YY_i}L^2\sqrt{\frac{m}{EI_{YY}}}$ where ω_{YY_i} is the ith natural circular frequency in the XZ plane under load and m the mass per unit length). Fig. 8, as well as Fig. 6, and Fig. 7, show that the method presented in this paper accurately reproduces the analytical model results presented in [47].
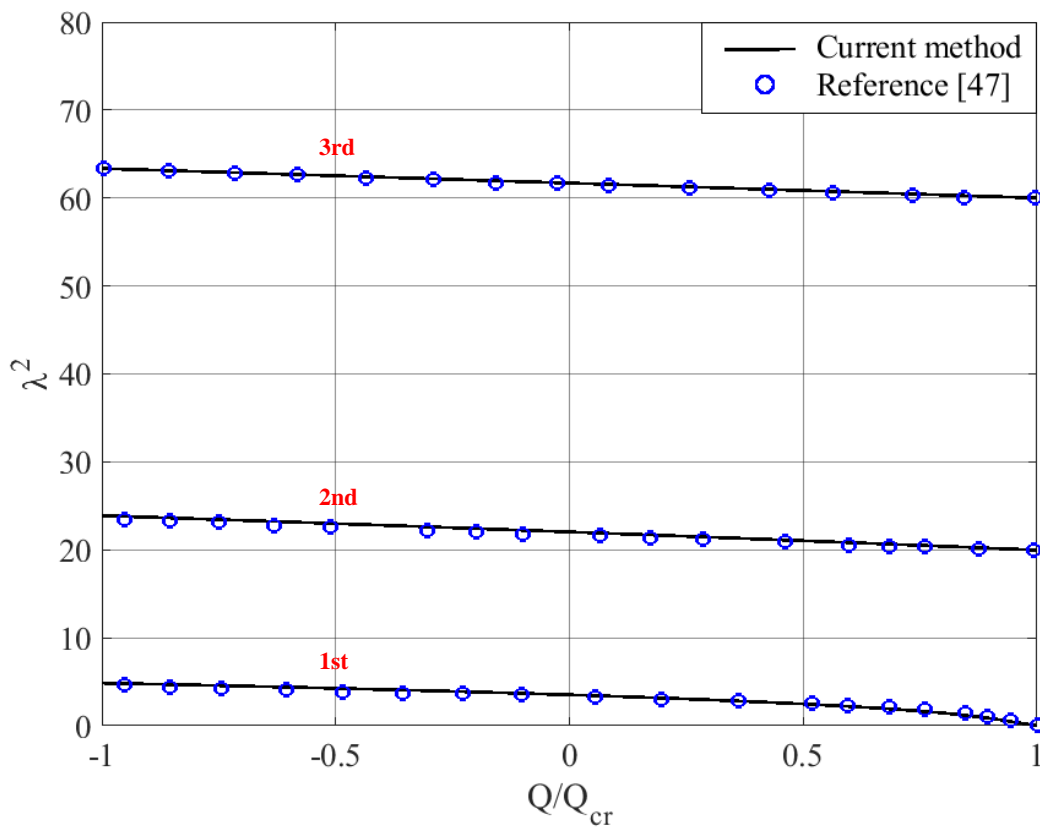
Fig. 8. Example 0 - non-dimensional frequencies of axially loaded cantilever beam (XZ-plane)

3.2 Example # 1 – Centrifugal Stiffening (Table 1)

In this example, a simple blade model consisting of a cantilever beam of rectangular cross section (Fig. 9) is used to validate the ability of the present method to calculate the natural

frequencies of the rotating beam under the effect of centrifugal stiffening. The results are compared to those obtained by Chen et al. [39] in 2016, who used a variational iteration method to study the flapwise vibration of rotating uniform Euler-Bernoulli beams. Non-dimensional natural frequencies were calculated in [39] and so, the dimensions of the beam are assumed as shown in Fig. 9, and the material properties of the beam are assumed as follows: density 7800 kg/m^3, Young Modulus 210 GPa, and Poisson ratio 0.28.
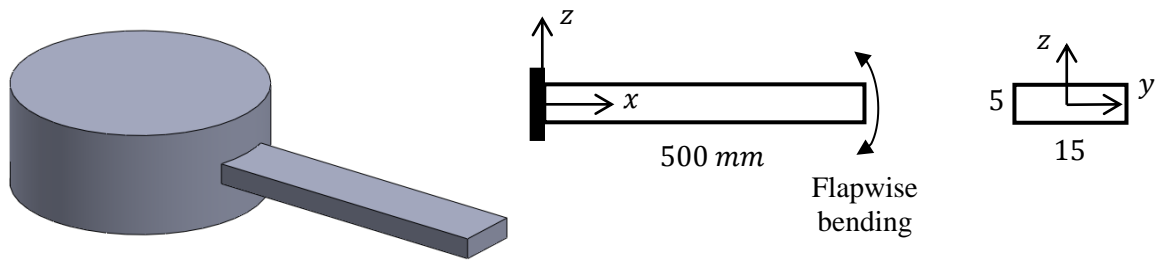
Fig. 9. Example 1 - Blade model used in [39]

Using the present method, the matrices **C**, **G**, $\mathbf{A}_1$, $\mathbf{A}_2$ in Eq. (44) were set to zero. The matrix **N** is as given by Eqs. (40a,b) with $\vartheta_{P_k} = 0$ and the number of divisions (points P_k) set to 500 (the hub radius was taken to be zero). Only the flapwise (*XZ* plane) modes were of interest since only these were considered in [39]. Hence, the matrices **D** and $\mathbf{H}_{\mathbf{m}_k}$ were a reduced form of Eqs. (50), (51) using only modes in the *XZ* plane:

$$\mathbf{D} = \text{diag}([\varpi_{YY_1} \quad \varpi_{YY_2} \quad \cdots \cdots]) \tag{62}$$

$$\mathbf{H}_{\mathbf{m}_k} = \begin{bmatrix} 0 & 0 & \cdots \cdots \\ -\dfrac{\mathrm{d}\phi_Z^{(1)}}{\mathrm{d}X} & -\dfrac{\mathrm{d}\phi_Z^{(2)}}{\mathrm{d}X} & \cdots \cdots \\ 0 & 0 & \cdots \cdots \end{bmatrix} \tag{63}$$

34

A total of $H = 10$ modes were used in the above equations. The data in the matrices $\mathbf{D}$ and $\mathbf{H}_{\mathbf{m}_k}$, were evaluated using the exact formulas given in [49].

Following [39], the natural frequencies solutions from the eigenproblem of Eq. (44) were converted to non-dimensional natural frequencies $\widetilde{\omega}_{YY_i}$ corresponding to the non-dimensional rotational speed $\tilde{\Omega}$:

$$\widetilde{\omega}_{YY_i} = \omega_{YY_i} L^2 \sqrt{\frac{m}{EI_{YY}}}, i = 1,2 ..., \quad \tilde{\Omega} = \Omega L^2 \sqrt{\frac{m}{EI_{YY}}} \tag{64a,b}$$

Table 2: Natural frequencies of blade model

Non-dim. speed	1st frequency			2nd frequency			3rd frequency		
	ref [39]	Present	%error	ref [39]	Present	%error	ref [39]	Present	%error
0	3.516	3.516	0	22.0345	22.0345	0	61.6972	61.6972	0
3	4.7973	4.8001	0.058	23.3203	23.325	0.020	62.985	62.9889	0.006
6	7.3604	7.3672	0.092	26.8091	26.8273	0.068	66.684	66.7013	0.026
12	13.1702	13.1873	0.130	37.6031	37.6728	0.185	79.6145	79.697	0.104

Table 2 presents a comparison with the results published in [39], where good agreement is demonstrated (maximum error 0.19%). The Campbell diagram of the first three flap-wise frequencies is presented in Fig. 10. The simulation time to generate this diagram was only 20 sec.

The above procedure was repeated using FE (with solid elements) to determine the zero-speed modal data in matrices $\mathbf{D}$ and $\mathbf{H}_{\mathbf{m}_k}$. The resulting Campbell diagram (Fig. 11) was virtually identical to that in Fig. 10, but took much longer to generate (35 min), time taken to find the closest FE nodes to each P_k point, in order to calculate angular displacement modal data from the FE translational displacement modal data for each of the 500 divisions using

35

the method of section 2.3. If beam elements were used in the FE, rather than solid elements, the method of section 2.3 would not be required (since beam elements have angular degrees of freedom). Table 3 shows that the maximum discrepancy relative to [39] increases to 1% since solid elements do not use the Euler-Bernoulli model of [39].
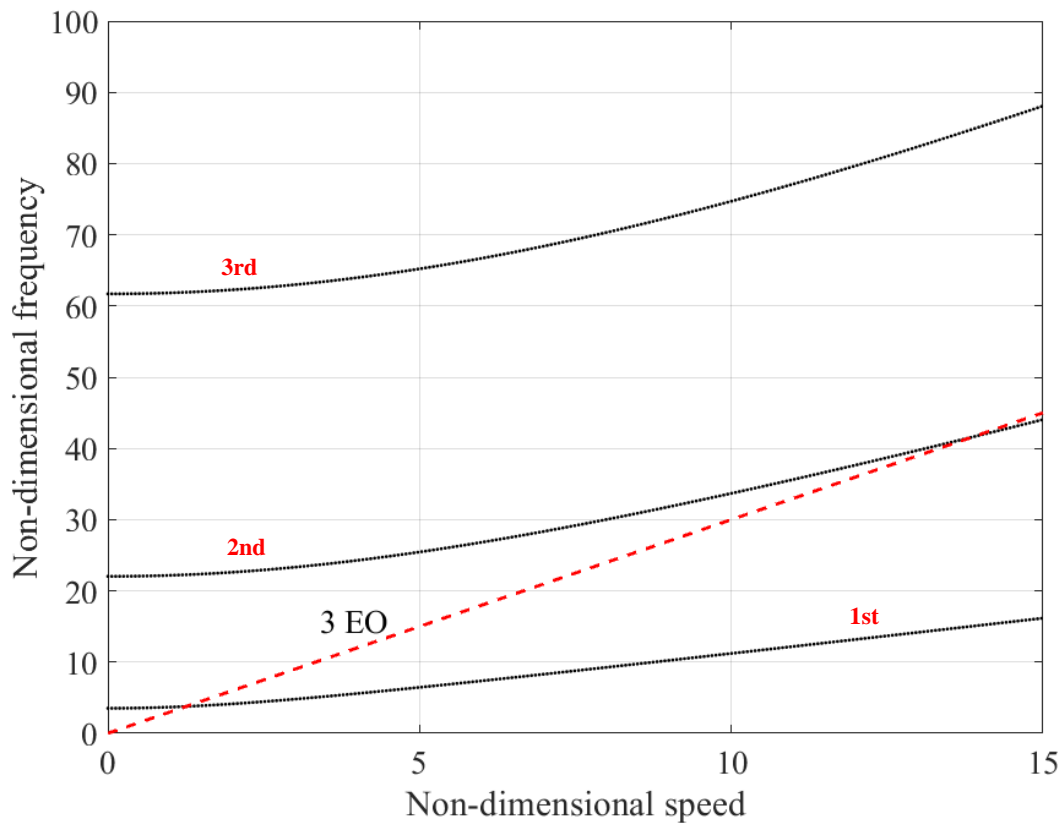

Fig. 10. Example 1 - Campbell diagram of blade model (using zero-speed modal data derived from analytical expressions)

Table 3: Natural frequencies of blade model (using zero-speed modal data from FE)

Nondim.	1st frequency			2nd frequency			3rd frequency		
speed	Ref [39]	Present	%error	Ref [39]	Present	%error	Ref [39]	Present	%error
0	3.516	3.5172	0.034	22.0345	21.9499	-0.384	61.6972	61.0543	-1.042
3	4.7973	4.814	0.348	23.3203	23.2662	-0.232	62.985	62.3351	-1.032
6	7.3604	7.3943	0.461	26.8091	26.845	0.134	66.684	66.0295	-0.982
12	13.1702	13.2362	0.501	37.6031	37.9795	1.001	79.6145	79.108	-0.636
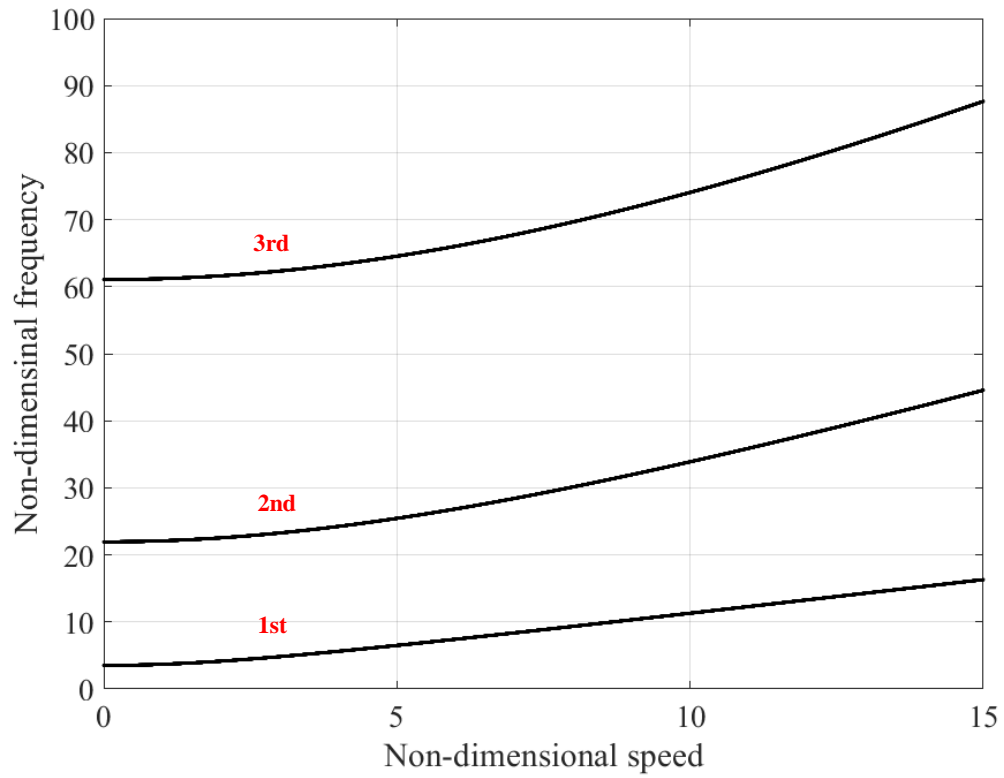
Fig. 11. Example 1 - Campbell diagram of blade model using zero-speed modal data derived from FE
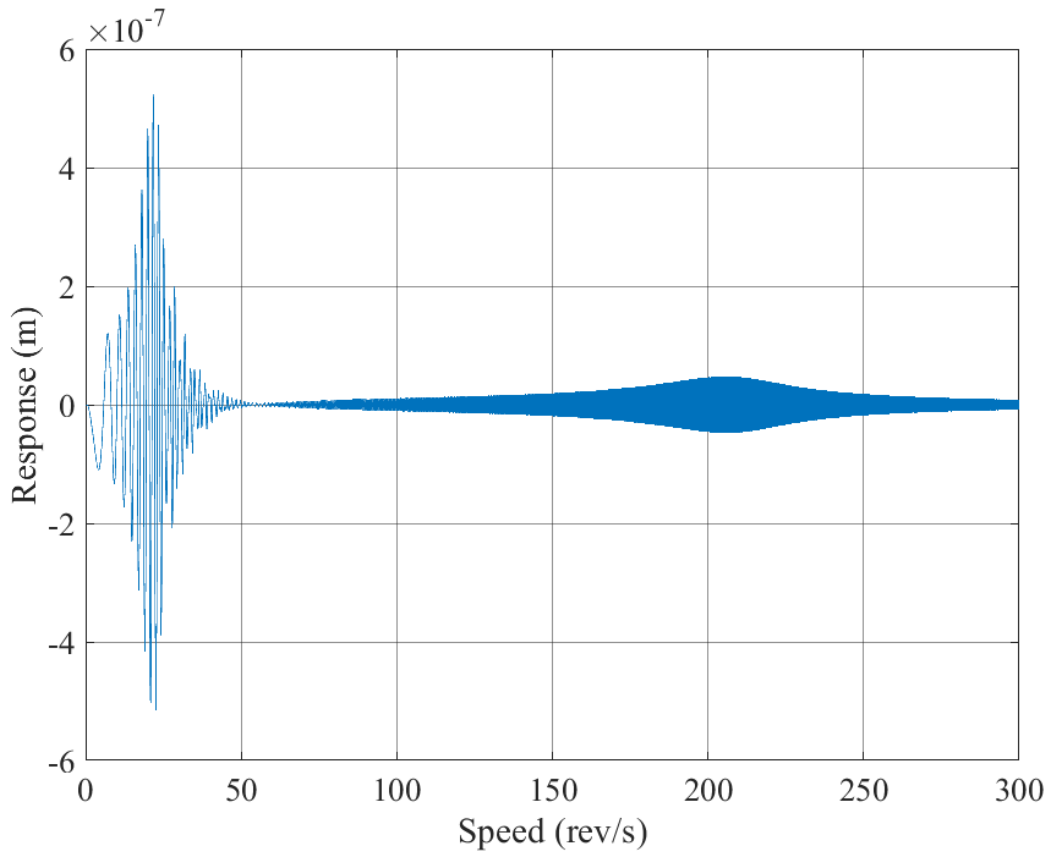
Fig. 12. Example 1 - forced response of blade model

A chirp excitation force was applied at one of the free end nodes in the Z-direction under variable speed conditions such that the excitation frequency was a fixed ratio (Engine Order, EO) of the rotational speed $\Omega(t)$:

$$f(t) = A \, \sin\left[\text{EO}\left(\Omega_i t + \left(\frac{\Omega_f - \Omega_i}{2T_s}\right)t^2\right)\right] \tag{65}$$

where Ω_i, Ω_f are the values of the initial and final angular speeds over a duration T_s. Fig. 12 shows the simulator response (as per section 2.4.2) for $A = 1$ and $\text{EO} = 3$ (i.e. "3EO excitation") and $T_s = 3$ sec, $\zeta_r = 0.05$ (Eq. (5)), where it is seen that the resonance speeds agree with the results from Campbell diagram.

3.3 Example # 2 – Coriolis Forces (Table 1)

Fig. 13 shows a blisk which was specially designed by Ruffini et al. [32] in 2015 for experimental and numerical (FE) analysis of Coriolis effects. It is modelled and analysed again here using the proposed method and the results are validated against the published results in [32].
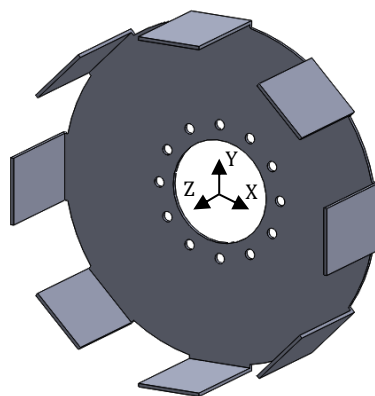
Fig. 13. Example 2: specially designed blisk for Coriolis effects validation, as used in [32]

As shown in Fig. 13, the blades are bent $90°$ (out-of-plane). According to authors of [32] this increased the Coriolis-induced frequency splits as much as possible in order to have distinct travelling wave modes. Such a design also minimised the effects of mistuning which could otherwise lead to frequency splits that overshadow the Coriolis effects. The horizontal leaning of the blades also makes centrifugal stiffening not noticeable [32].

Detailed dimensions and boundary conditions of the model were not available in [32], so a number of attempts have been made with different dimensions until accurate natural frequencies of the non-rotating blisk were obtained. The zero-speed modal data were obtained by ANSYS with the nodes along the periphery of the central hole and the small holes assumed fixed. The number of degrees of freedom used for zero-speed modal data computation was 662337.

In Eq. (44), all the matrices were set to zero except D and A_1. The number of basis modes $H = 10$. The number of rotational inertia divisions (points P_k) used in this matrix (Eq. (39)) was 54. Each blade divided into a 3 divisions in axial direction (not radial, due to their bent), and the disk inertia was divided into 30 divisions [See Appendix A].

The Campbell diagram generated using the new method is shown in Fig. 14 for mode nos. 1 to 7 over the speed range 0-500 rpm. The simulation time was only 10 sec. The experimental results obtained in [32] are reproduced in Fig. 14 and good correlation with the predictions is evident, proving the validity of the new method. The critical speeds for single engine order are shown in Table 4.

Table 4: Critical speeds (current method)

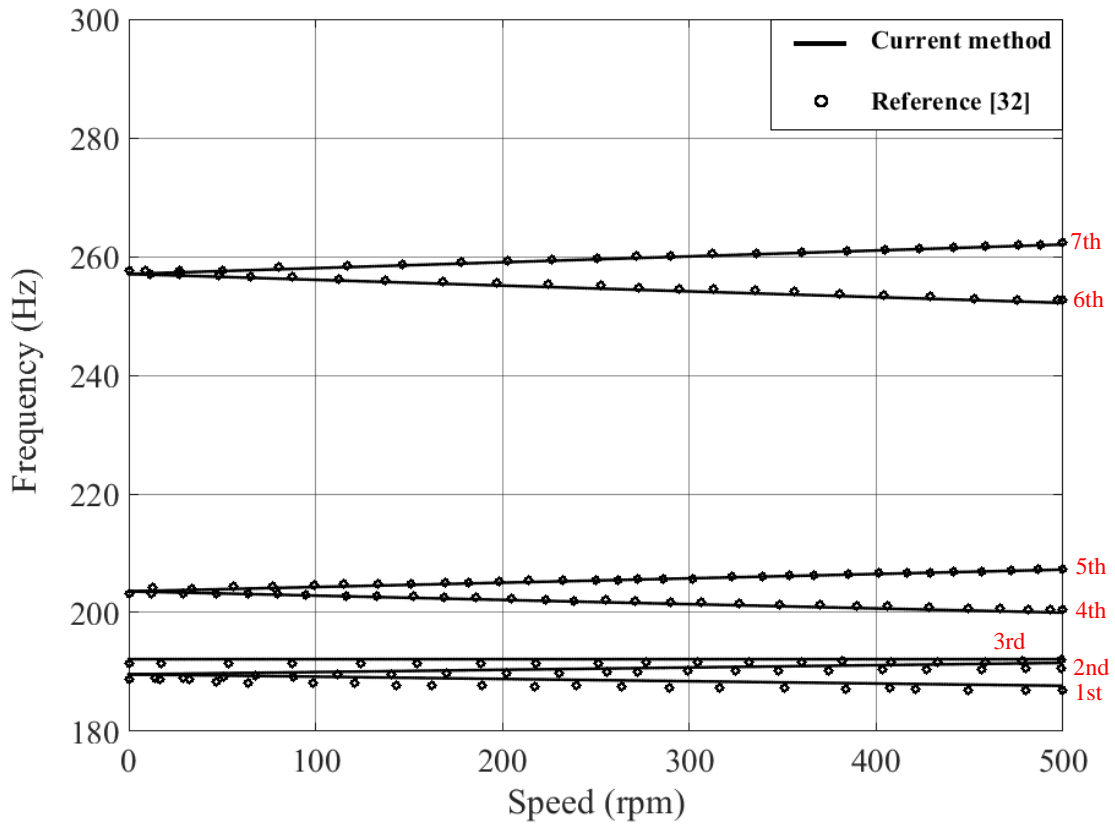| Mode #	1	2	3	4	5
Critical speed (rev/s)	148.9	156.8	174.2	192.15	258.7

Fig. 14. Example 2 - Campbell diagram of the blisk specially designed for Coriolis effects
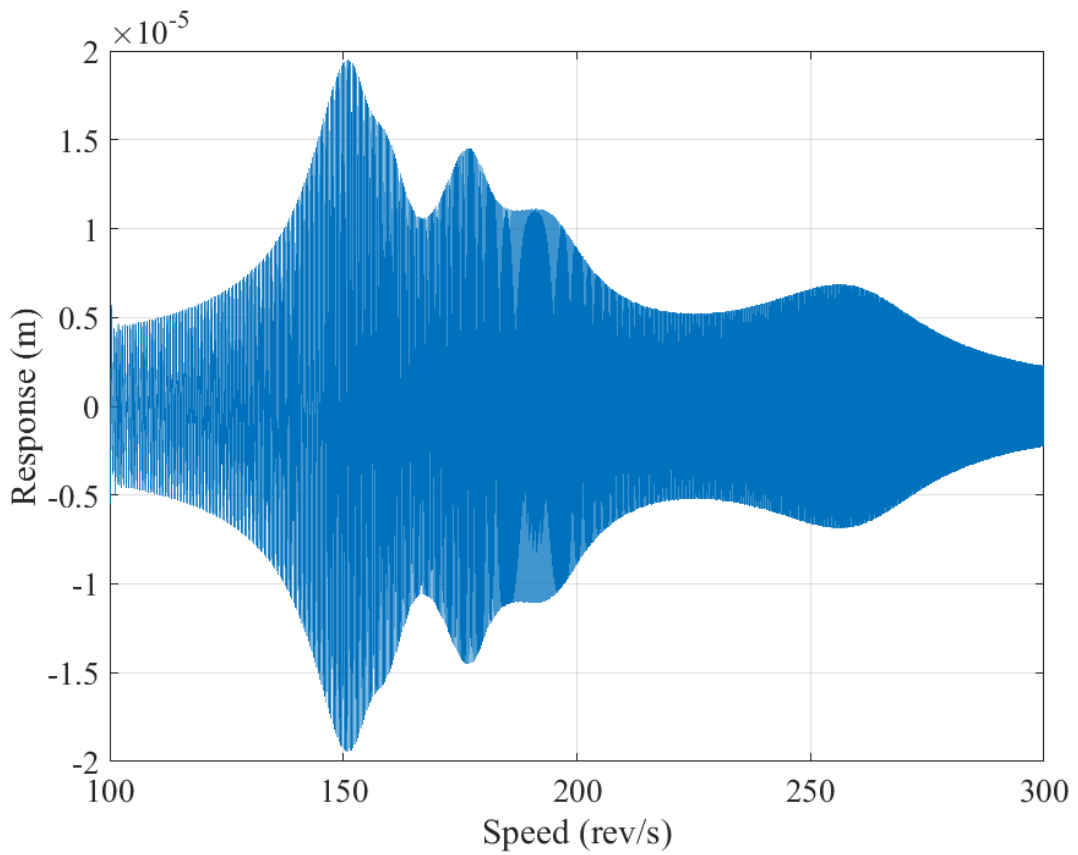

Fig. 15. Example 2 - forced response of the blisk specially designed for Coriolis effects

40

A chirp excitation force was applied at one of the blade tips (normal to the blade) under variable speed condition, as per Eq. (56). Fig. 15 shows the simulator response (as per section 2.4.2) for $A = 1$ and $EO = 1$ and $T_s = 4 \sec$, $\zeta_r = 0.05$ (Eq. (5)). The resonance speeds agree with the Campbell diagram results with small percentages of errors since the response is transient and not strictly steady-state.

3.4 Example # 3a,b – Gyroscopic Effect

3.4.1 Example # 3a – Gyroscopic moment – effect of disk flexibility (Table 1)
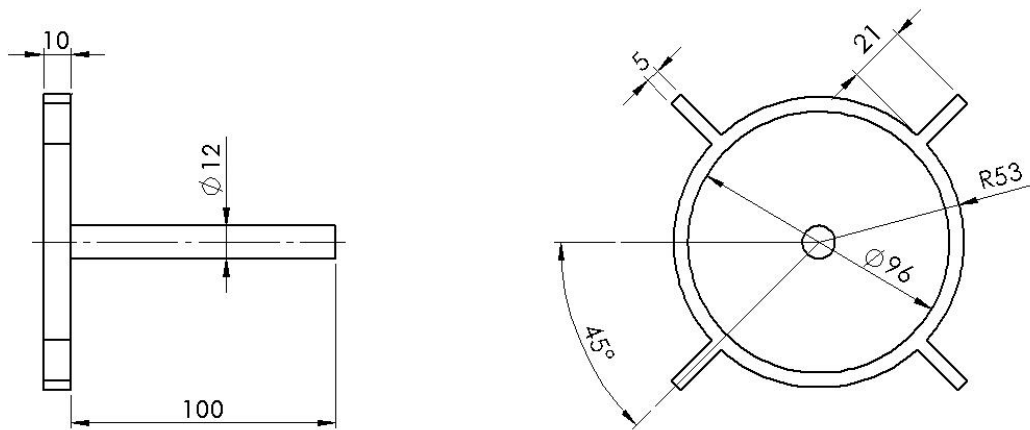
Fig. 16. Example 3a - blisk supported by free-fixed shaft

The model shown in Fig. 16 consists of a disk with 4 blades positioned at the end of a cantilevered shaft. It is therefore subjected to gyroscopic coupling which leads to splits in frequencies with increasing rotational speed. The model was created using *SolidWorks* and *ANSYS*, the material used was steel with 7850 kg/m³ density and 200 GPa elasticity modulus. The disk is considered bonded to the shaft, and the number of DOF used to generate the zero-speed modal data was 134217.

41

The first five zero-speed natural frequencies and mode shapes are shown in Fig. 17 and Table 5. It is clear from Fig. 17 that modes 1, 2, 4, and 5 are bending modes, so they are more likely to be affected by gyroscopic moments (resulting in frequency splits).
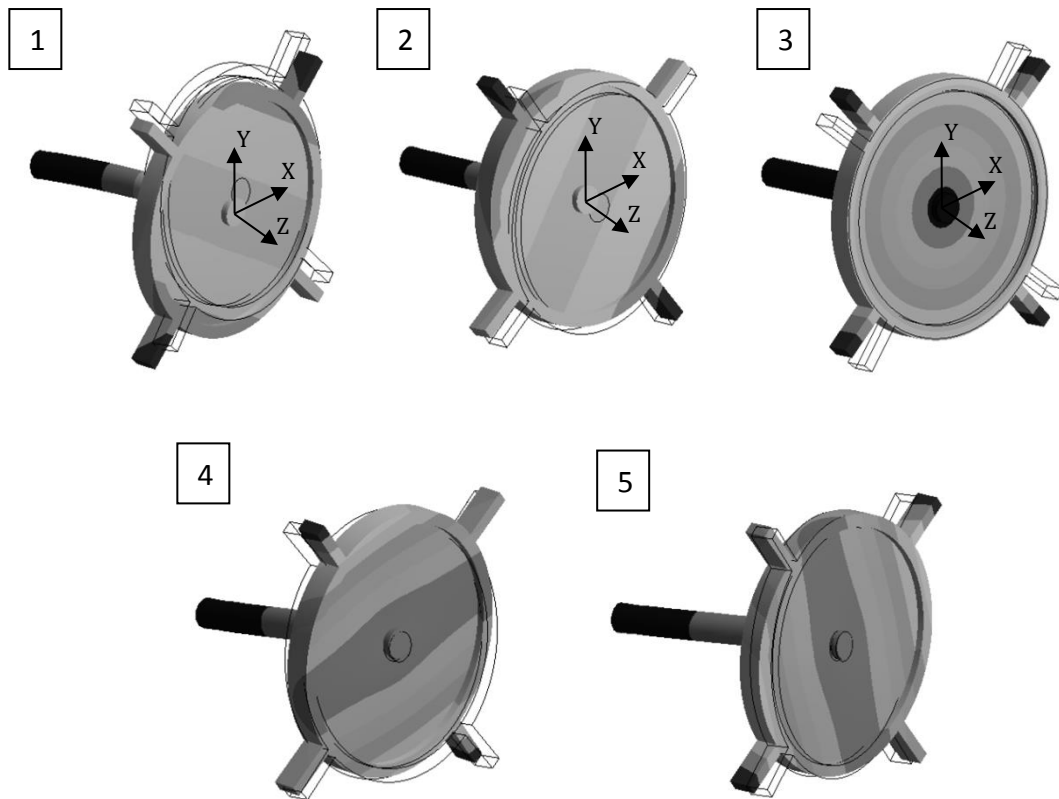

Fig. 17. Example 3a - zero-speed mode shapes of blisk supported by free-fixed shaft

Table 5: Natural frequencies blisk supported by free-fixed shaft at zero speed

Mode #	1	2	3	4	5
Natural frequency (Hz)	171	171	231	611	611

Another modal analysis was carried out using the rotordynamics analysis facility in *ANSYS* over a rotational speed range 0-600 rev/s, and the Campbell diagram was extracted as shown

in Fig. 18. In this *ANSYS* analysis, the gyroscopic effect was activated on its own (without Coriolis and spin softening effects added) by applying the CORIOLIS command in a stationary reference frame [40].
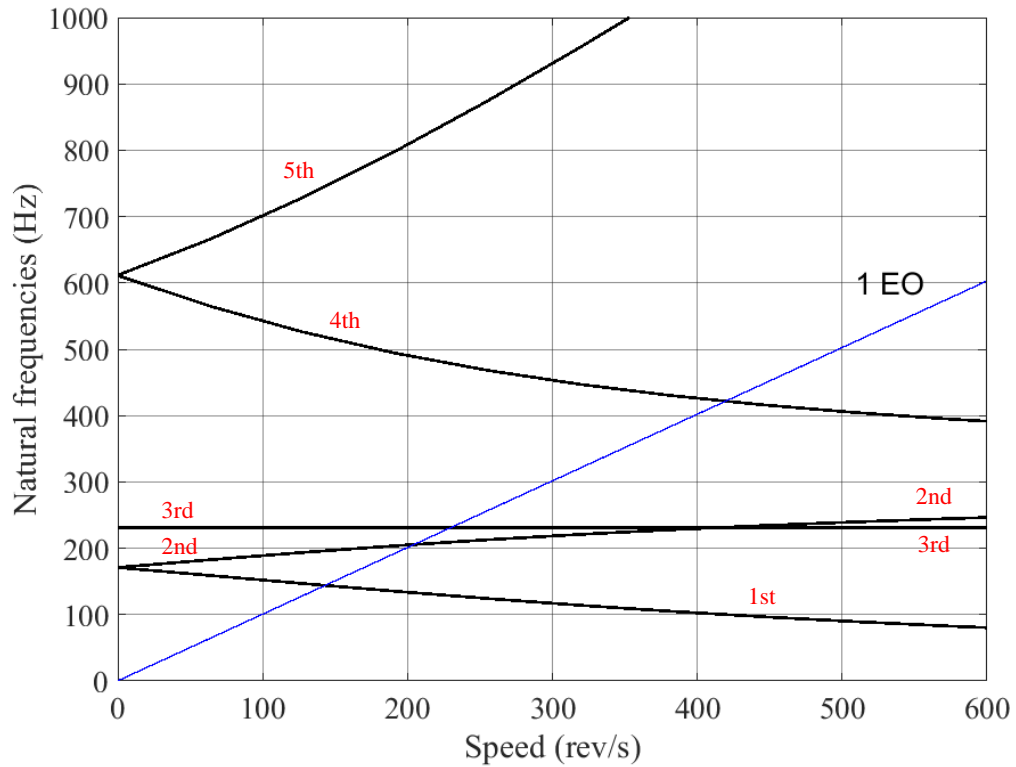
Fig. 18. Example 3a - Campbell diagram of rotating blisk supported by free-fixed shaft using *ANSYS* rotordynamic solver.

As expected, Fig. 18 shows that modes 1, 2, 4, and 5 are affected by gyroscopic moments due to bending of both shaft and disk. Frequency splitting was high for modes 4 and 5 due to the bending of the disk. As seen from Fig. 18, for 1 EO excitation (i.e. EO = 1, Eq. (56)), only four critical speeds exist in the selected range of speeds and these are listed in Table 6.

Table 6 Critical speeds (1 EO excitation) of blisk supported by free-fixed shaft (*ANSYS* rotordynamics solver).

Mode #	1	2	3	4	5
Critical speed (rev/s)	143.9	205.8	230.7	421.5	-

The Campbell diagram was then generated by the new method, as per section 2.4.1, using the zero-speed modal data (Fig. 17). All the matrices in Eq. (44) were set to zero except **D** and **G**. The number of basis modes $H = 5$. Initially, the blisk was assumed to be rigid as far as the gyroscopic effect was concerned i.e. the matrices $\mathbf{H}_{\mathbf{g}_k}$ were assumed identical for all points P_k on the (rigid) blisk, as explained under Eq. (27) i.e. the modal displacements $\psi_{\theta_{x_{P_k}}}^{(r)}$, $\psi_{\theta_{y_{P_k}}}^{(r)}$ were all equal to the values at hub (i.e. were purely due to the flexibility of the shaft). The resulting Campbell diagram (Fig. 19) correlates well with the *ANSYS* result only for mode nos. 1 and 2 (where the bending is mainly in the shaft, Fig. 17), and of course mode 3 (not affected by gyroscopic effect since it is torsional, Fig. 17). For modes 4 and 5 (where the zero-speed modes are dominated by flexibility of the disk, Fig. 17), Fig. 19 shows that the Campbell diagram by the new method with rigid gyroscopic effect assumption is in disagreement with the *ANSYS* rotordynamics solver result. This observation is also evident when comparing the critical speeds predicted by the new method (rigid disk gyroscopic effect assumption) with those from the ANSYS rotordynamics solver (Table 7), where the errors are low except for the fourth critical speed (28.7%).

Table 7: Critical speeds (1 EO excitation) of blisk supported by free-fixed shaft (new method, rigid assumption for disc gyroscopic effect)

Mode #	1	2	3	4	5
Critical speed (rev/s)	146.8	208.5	230.5	542.5	-
% discrepancy from *ANSYS* rotordynamics solver	2	1.3	-0.1	28.7	-

Fig. 20 shows the result of the Campbell diagram analysis by the new method when flexibility of the disk is considered (i.e. the matrices $\mathbf{H}_{\mathbf{g}_k}$ were allowed to be different for

different points P_k on the blisk). In this case, 42 inertia subdivisions (Fig. 2) were used for the blisk [See Appendix A]. It is evident that the correlation between the Campbell diagrams of the *ANSYS* rotordynamics solver and the proposed method (Fig. 20) for mode nos. 4 and 5 is considerably improved relative to previous result (Fig. 19). Table 8 shows that the error in 4th critical speed becomes just 1.8%. Errors in mode 1st and 2nd critical speeds slightly increased due to errors in the calculations of the angular modal displacements from the translational modal displacements by the vector product method of section.
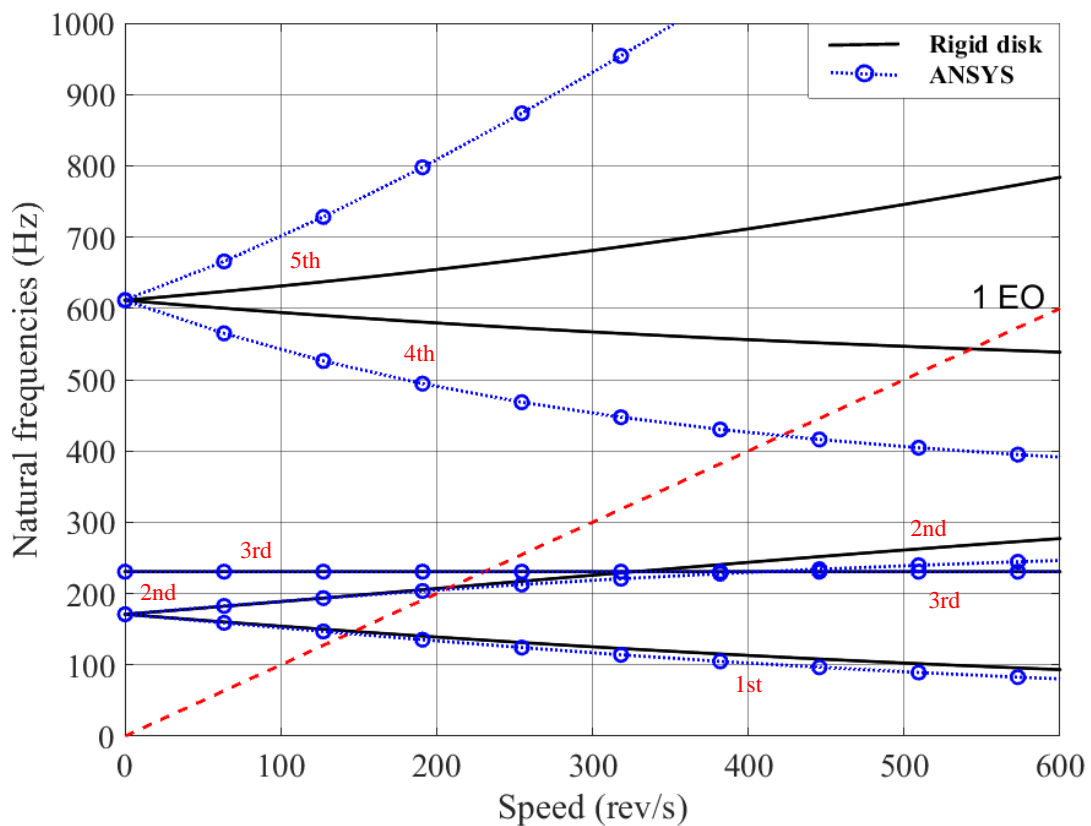
Fig. 19. Example 3a - Campbell diagram of rotating blisk supported by free-fixed shaft using the proposed method with gyroscopic effect based on rigid disc assumption.

An important advantage of the new method is the ability to produce the Campbell diagram (including gyroscopic effect with disk flexibility) in less than 1 minute with high resolution (1000 points) compared to about 2 hrs for just 11 points using *ANSYS* rotordynamic solver.
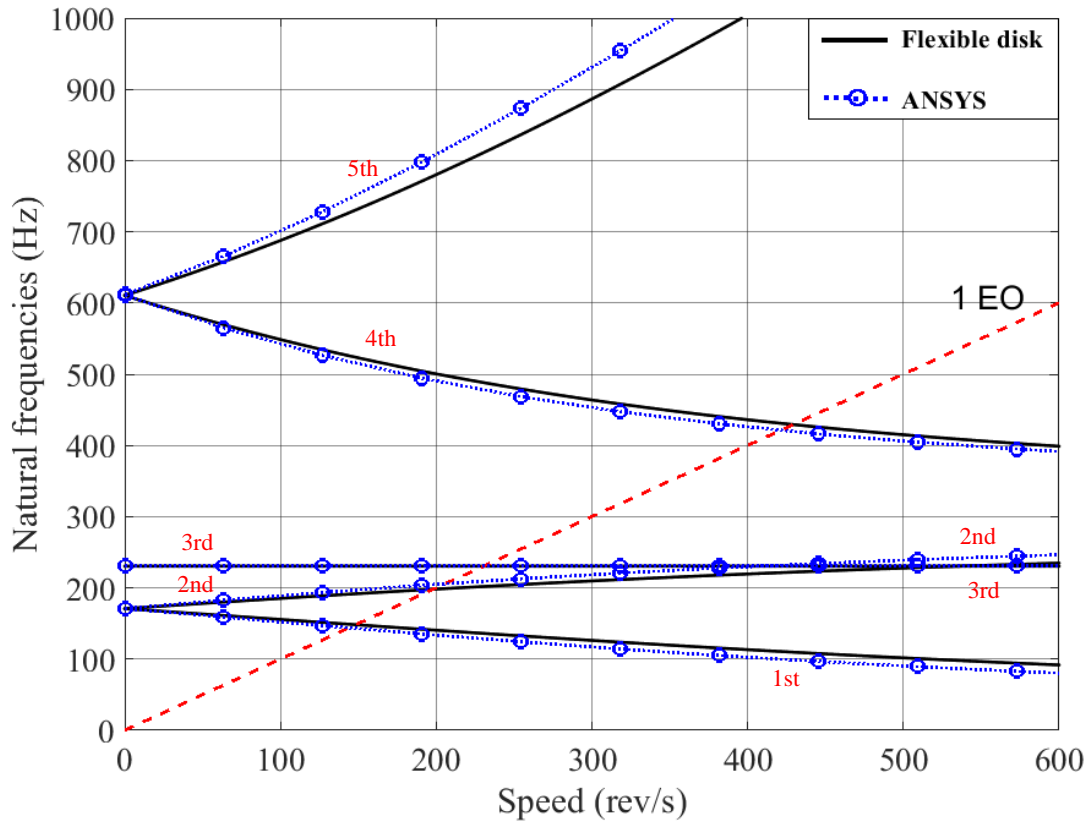
Fig. 20. Example 3a - Campbell diagram of rotating flexible blisk supported by free-fixed shaft using the proposed method with gyroscopic effect based on flexible blisk.

Table 8: Critical speeds (1 EO excitation) of flexible blisk supported by free-fixed shaft (new method, gyroscopic effect with blisk flexibility)

Mode #	1	2	3	4	5
Critical speed (rev/s)	148.3	198.1	230.4	429.3	-
% discrepancy from *ANSYS* rotordynamics solver	3	-3.7	-0.1	1.8	-

3.4.2 Example # 3b – Gyroscopic moment – example from literature (Table 1)

A model of a flexible shaft supported by 2 rigid bearings and a bladed disk of 8 blades shown in Fig. 21 was analysed by Chun and Lee in 1996 [18]. In their analysis, the supports were

modelled as pivots (i.e. the bearing flexibility was neglected), the shaft was modelled as a beam of different cross-sections, the disk as a uniform circular plate, and the blades as uniform rectangular beams. For the case referred to as "model 1" in [18], the blades had no pre-twist and no stagger, and the results were validated against FE and experimental results published by Zhang et al. in 1994 [48]. The same case shall be analysed in this section by the method of this paper.
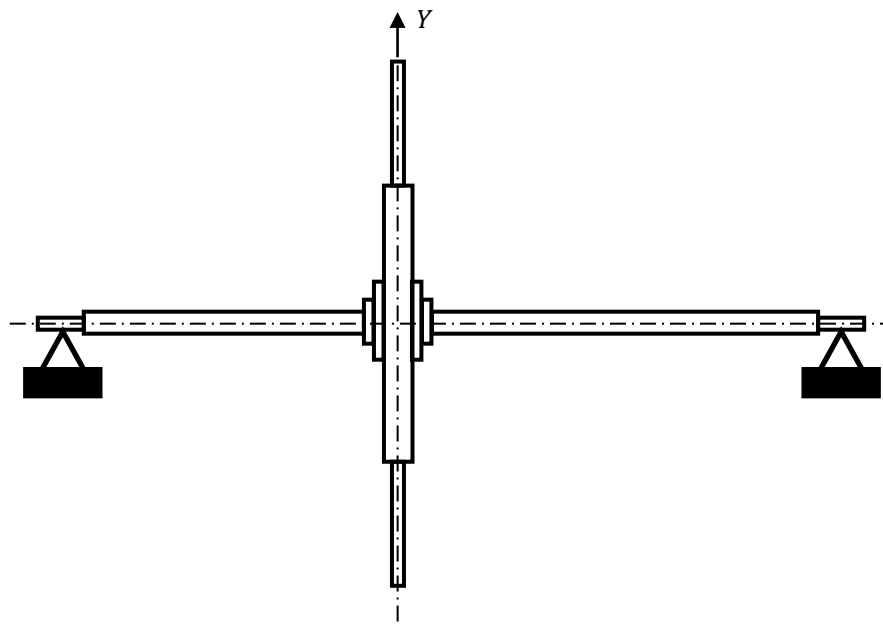

Fig. 21. Example 3b: a model of a bladed disc carried by shaft supported by 2 rigid bearings, as considered in [18].

The material properties used for the assembly are: density $7850\,\mathrm{kg/m^3}$, Young Modulus $210\,\mathrm{GPa}$, and Poisson ratio 0.28. The zero-speed modal data were generated by *ANSYS* using solid elements and the natural frequencies are listed in Table (9), along with the corresponding results of [18] and [48].

The Campbell diagram was generated using the present method as shown in Fig. 22. All the matrices in Eq. (44) were set to zero except **D** and **G**, and the number of basis modes $H = 8$. 54 inertia subdivisions (Fig. 2) were used for the blisk [See Appendix A]. The Campbell diagram generated by the present method agrees fairly well with that published in [18].

Table 9: Zero-speed natural frequencies

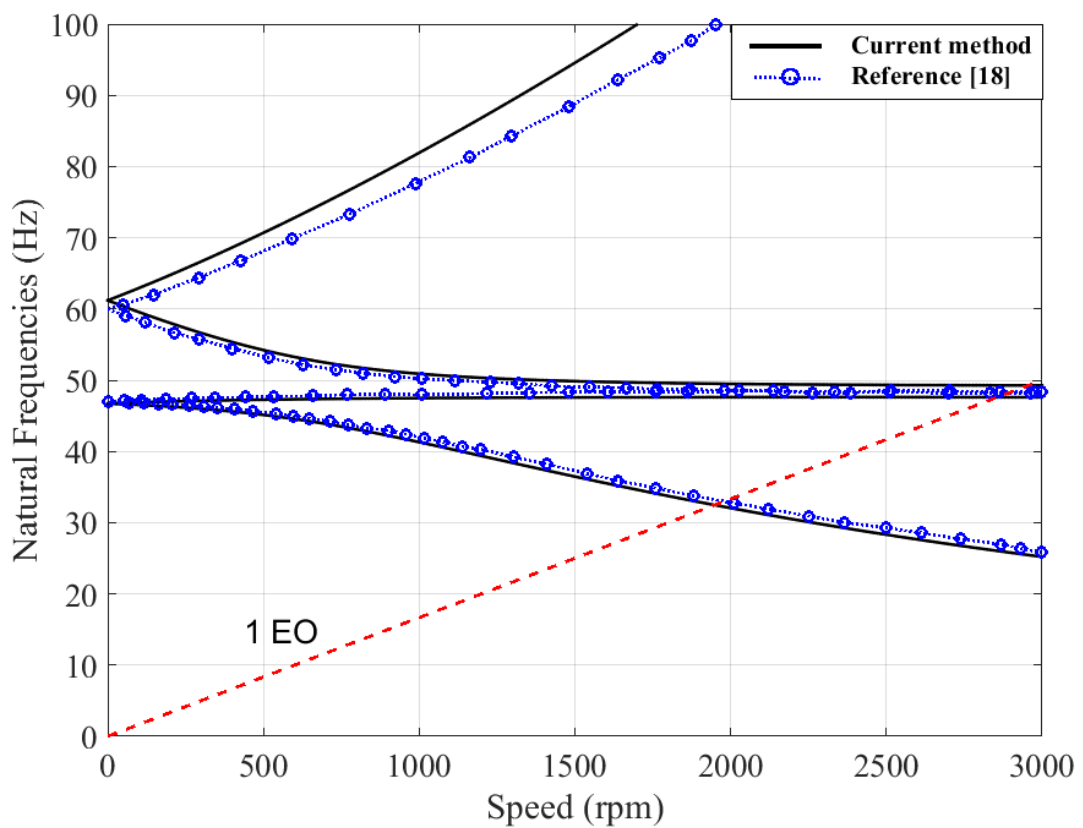| Method	Natural frequency (Hz)			
	1	2	3	4
FE [present work]	46.8	46.8	61.3	61.3
Analytical [18]	47.17	47.17	59.92	59.92
FE [48]	46.0	46.0	60.15	60.15
Experimental [48]	48.0	48.0	-	-

Fig. 22. Example 3b - Campbell diagram of system in Figure 21 using proposed method.

A travelling wave excitation was then applied to the blade tips under a steadily increasing speed condition and at fixed engine order (EO). In this type of excitation, the force on the tip of blade no. *n* is given by [51]:

$$f_n(t) = A \, \sin\left[\text{EO}\left(\Omega_i t + \left(\frac{\Omega_f - \Omega_i}{2T_s}\right)t^2\right) + \frac{2\pi n N_d}{N_b}\right] \tag{66}$$

where N_b is the total number of blades, and N_d is the number of nodal diameters. Fig. 23 shows the simulator response (as per section 2.4.2) at one of the blade tips in the *x*-direction for $A = 1$ and $\text{EO} = 1$ and $T_s = 2$ sec , $\zeta_r = 0.05$ (Eq. (5)). The figure shows that the resonances due to the excitation of the first, second, and third modes agree with the first three critical speeds (for 1EO excitation) indicated in Fig. 22.
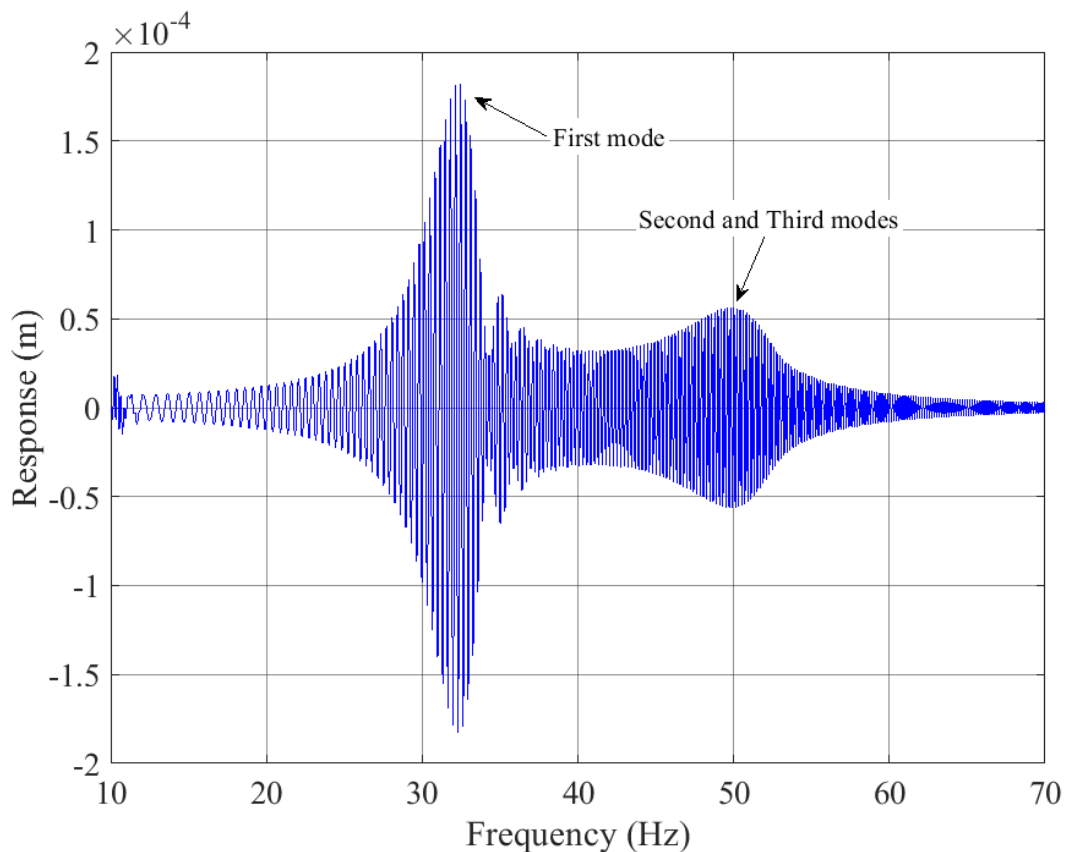
Fig. 23. Example 3b – Forced response of system in Figure 20 using proposed method.

3.5 Example # 4 – Gyroscopic, Coriolis, Spin Softening, Centrifugal Stiffening

The system shown in Fig. 24 was first solved for the modal data by Ma et al. [2] in 2015. They examined the effects of rotation analytically, numerically (FE), and experimentally. Not all natural frequencies were validated experimentally, so only those validated by experiments will be considered here. In their analytical analysis the authors in [2] used Hamilton's principle in conjunction with the assumed modes method.
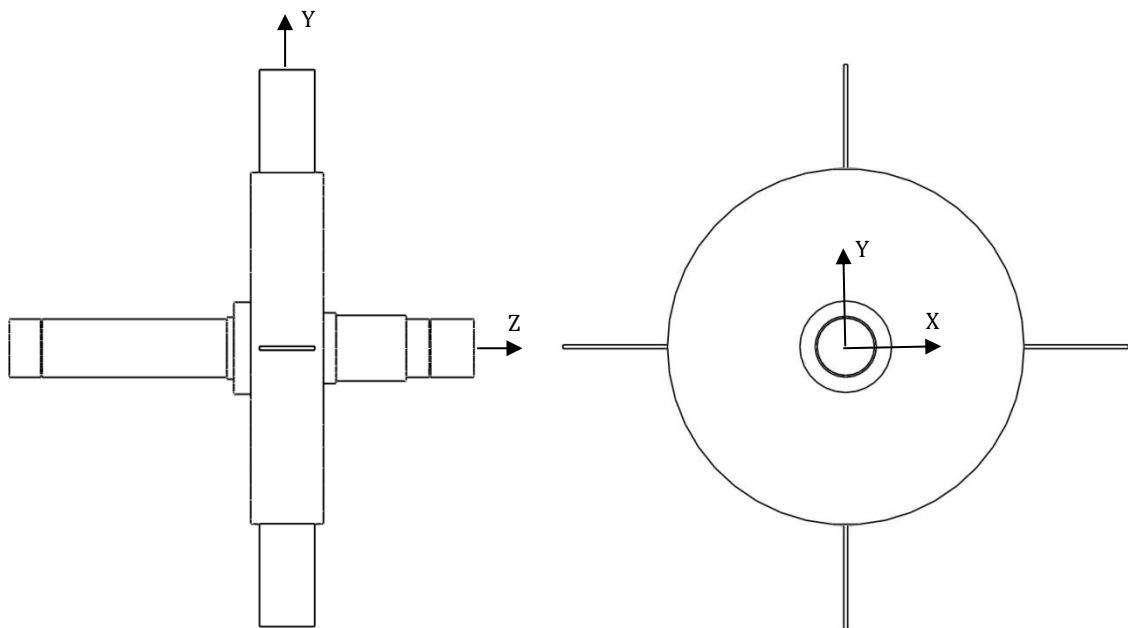

Fig. 24. Example 4 - rotating assembly considered in [24]

The system consists of a stepped circular cross-section shaft supported by two bearings (with equal stiffness in the vertical and horizontal direction 1.5×10^7 N/m) carrying a disk with four blades, the material is the same for all components (density 7800 kg/m^3, Young Modulus 200 GPa). *SolidWorks* and *ANSYS* used to create the FE model for the zero-speed data. The mesh was refined on all blades and the outer surface of disk in order to improve the results, and the total number of degrees of freedom was 1800858. The boundary conditions were as follows: both ends of the shaft were constrained from axial motion; left hand end constrained from torsional motion. Fig. 25 shows the mode shapes of the system at zero

speed, as obtained by *ANSYS*. The zero-speed natural frequencies are presented in Table 10 where they are also compared with the results published in [2].
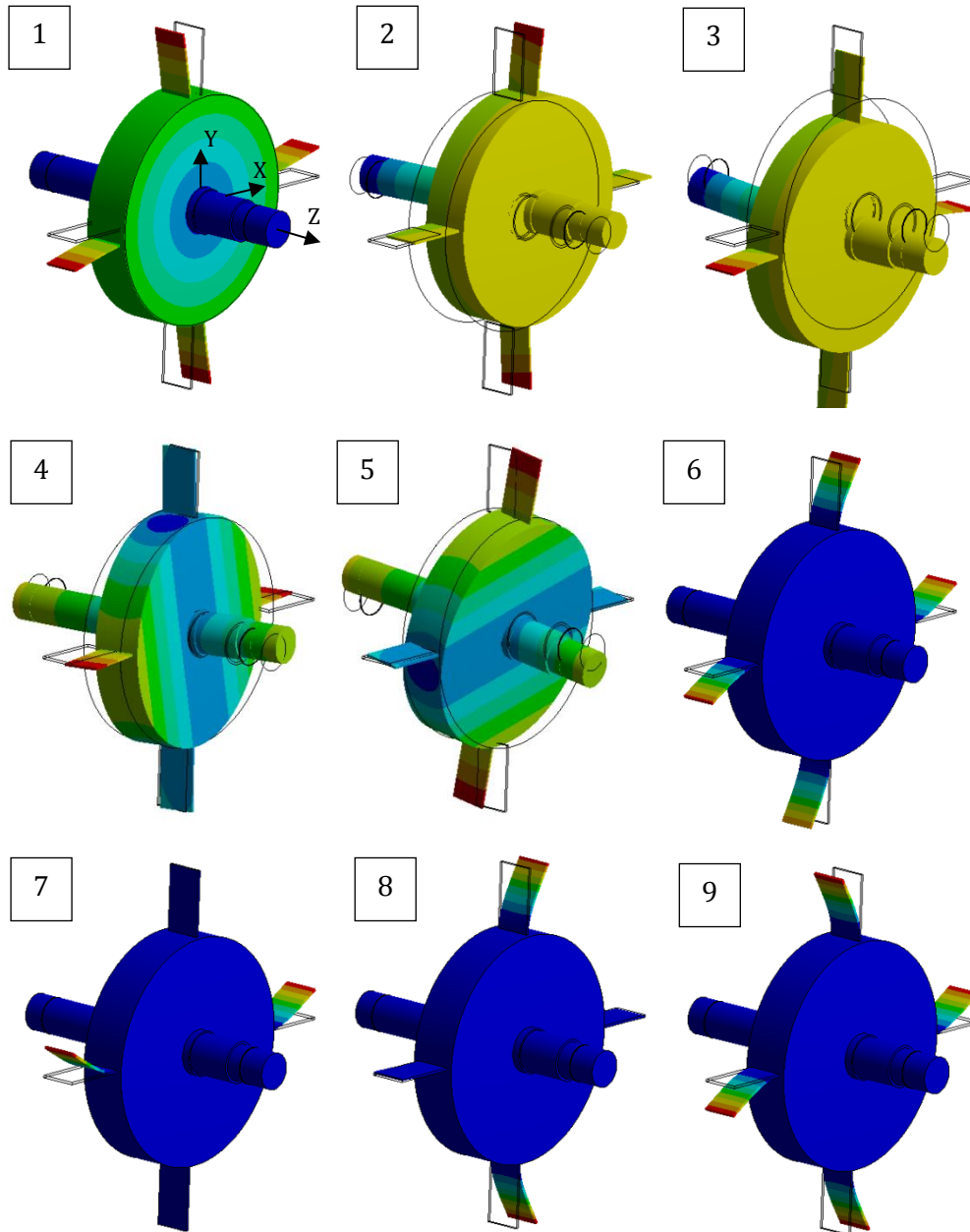

Fig. 25. Example 4 - mode shapes of the non-rotating assembly.

Table 10: Natural frequencies of the non-rotating assembly.

Mode	1	2	3	4	5	6	7	8	9
FE [present] (Hz)	121.7	133.8	133.8	266.5	266.5	364.3	365	365	370.4
FE [2] (Hz)	117.4	132.9	132.9	269.6	269.6	364.7	365.4	365.4	370.7
Experimental [2] (Hz)	-	129.3	129.3	258	258	361.3	364.7	368	372

The zero-speed modal data were then used in the proposed method in order to generate Campbell diagram as per section 2.4.1. The number of basis modes $H = 9$. The number of inertia divisions is 42 [See Appendix A]. First, only the gyroscopic effects were considered, as shown in Fig. 26. It is clear that the affected modes were those featuring some inclination of the disk (Fig. 25): the 2nd, 3rd modes (slightly affected) and the 4th, 5th modes (highly affected). This agrees with what was reported in [2].
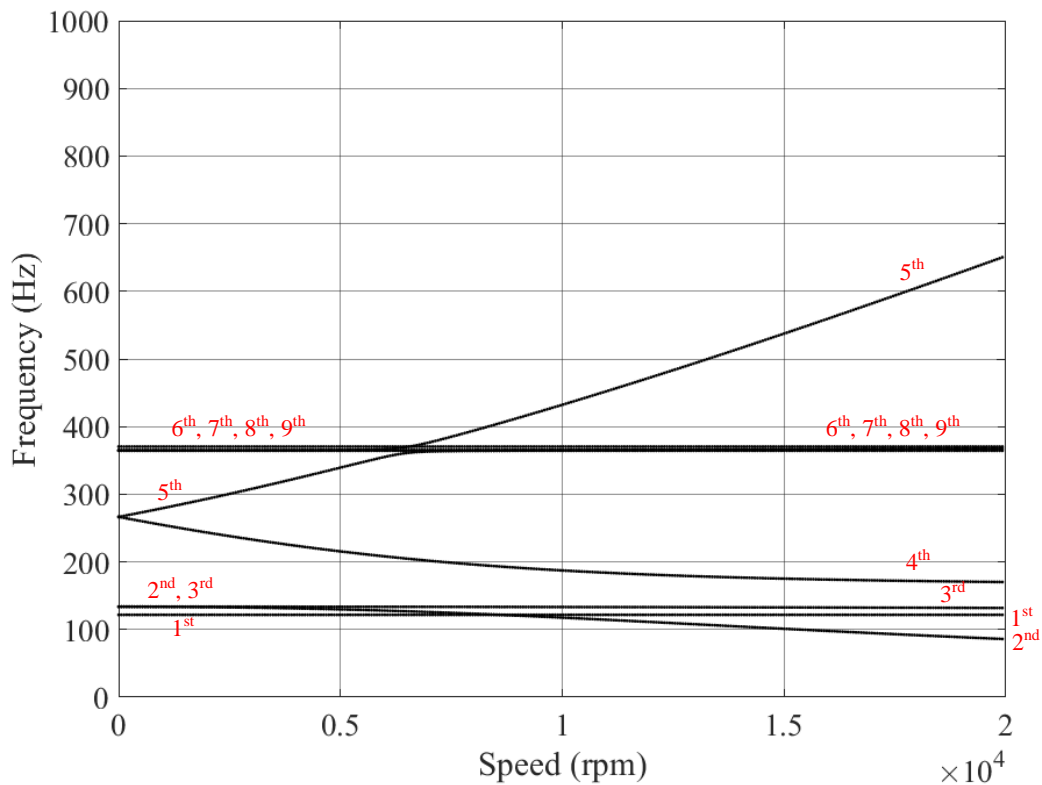

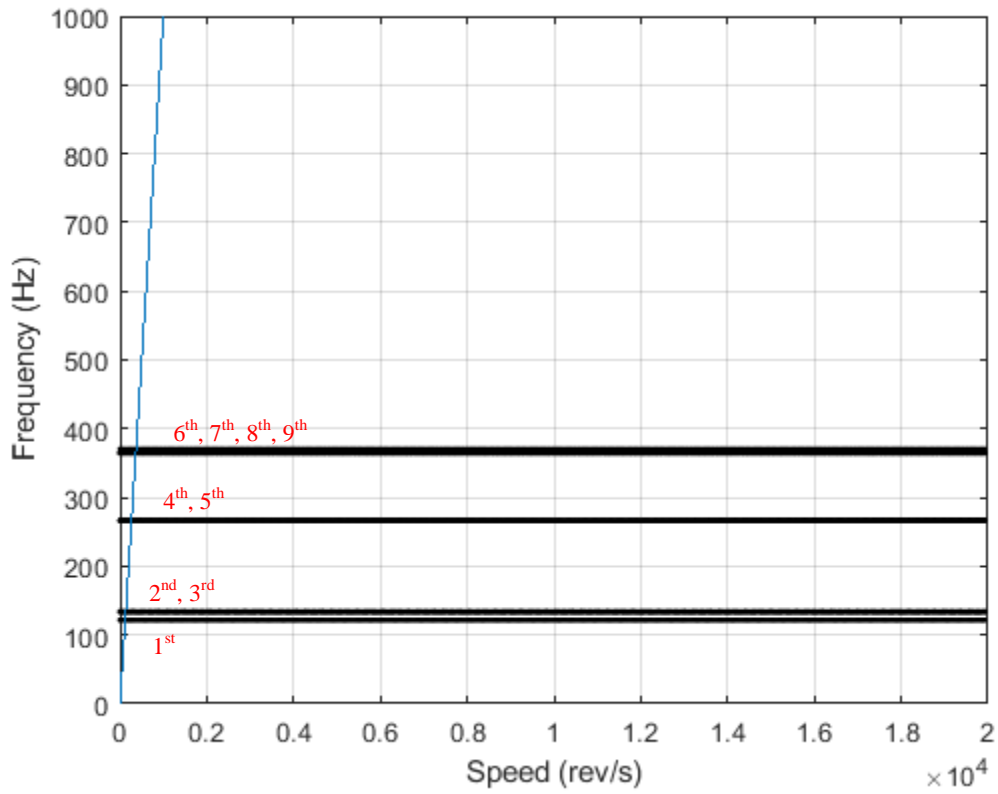Fig. 26. Example 4 - Campbell diagram with gyroscopic effect only.

52

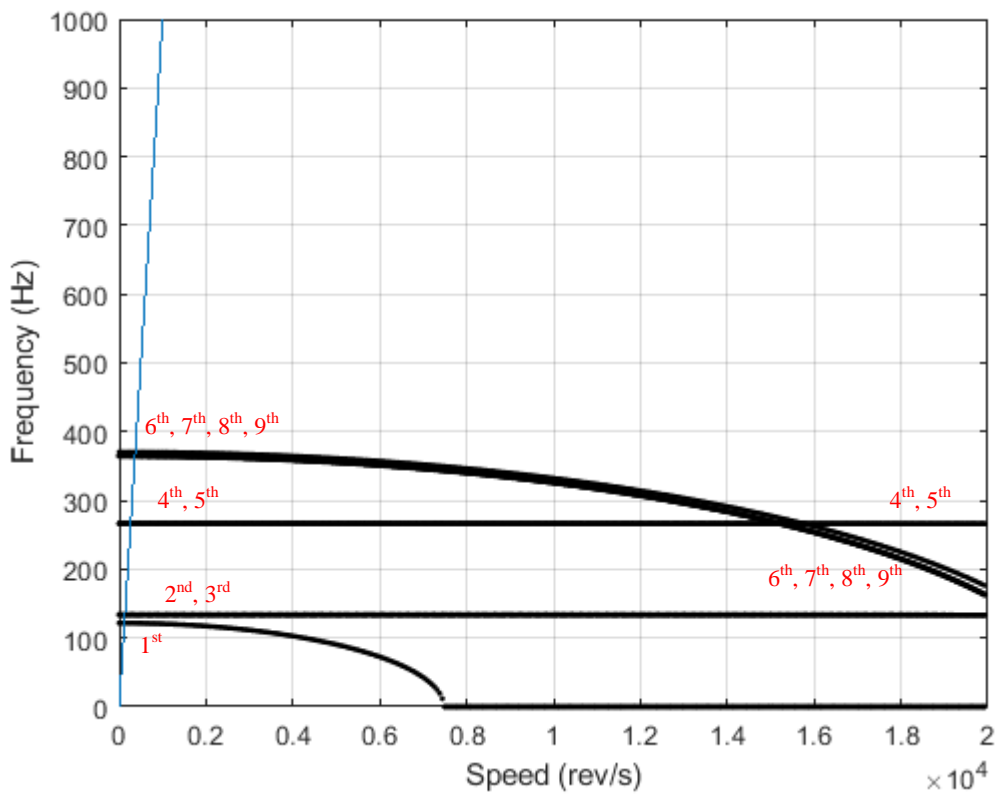Fig. 27. Example 4 - Campbell diagram with Coriolis effect only.

Fig. 28. Example 4 - Campbell diagram with spin with softening effect only.
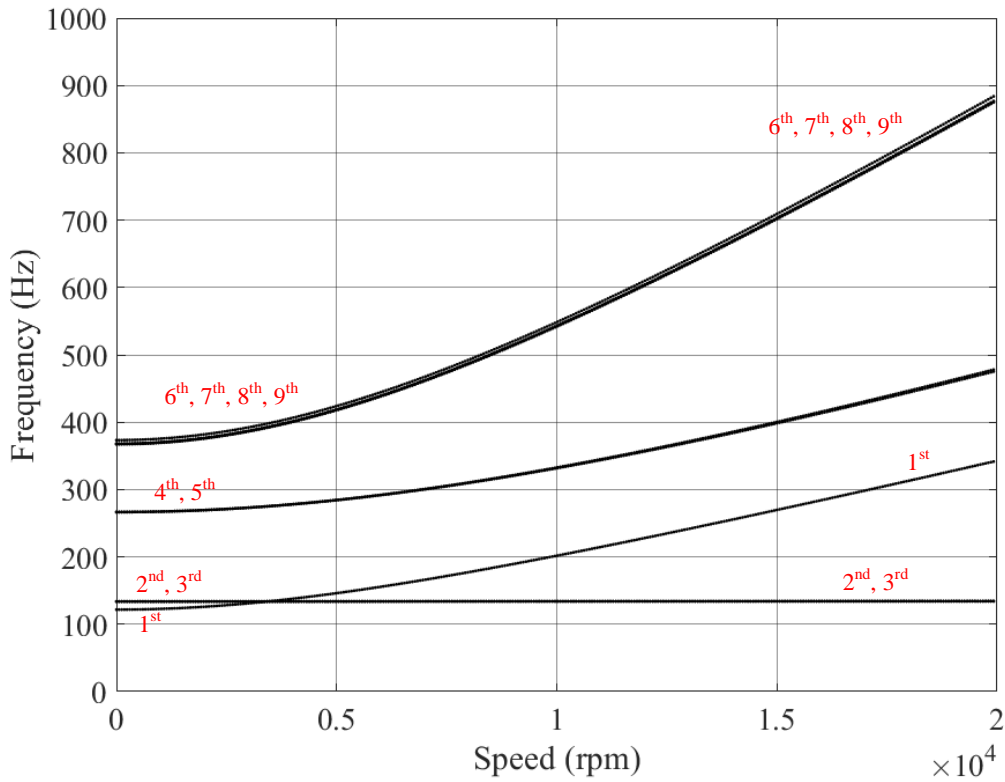
53

Fig. 29. Example 4 - Campbell diagram with centrifugal stiffening effect only.

Secondly, the effects of Coriolis only (Fig. 27) and spin-softening only (Fig. 28) were examined. It is clear that in case of Coriolis, no modes are affected, which justifies the assumption made in [2] of neglecting Coriolis. In case of spin-softening, mode nos. 2-5 are unaffected, which justifies another assumption made in [2] that spin-softening effects came only from the blades (the affected modes 1, 6-9 involve little or no bending vibration in either shaft or disc, as per zero-speed modes in Figure 25).

The 3rd trial included the centrifugal stiffening effects, where the effects of the individual components (M_x, M_y, M_z) of the centrifugal stiffening moment $\mathbf{m}_k$ (Eq. (20)) were examined. By examining the zero-speed mode shapes in Fig. 25, it is clear that mode no. 6 is the only mode affected by M_x, and mode no. 4 is the only mode affected by M_y. The modes affected by M_z are mode nos. 1, 6-9. Hence, considering all three components of $\mathbf{m}_k$, all modes would be affected except for the 2nd and 3rd, as shown in Fig. 29.

The last step was to consider all effects at the same time and comparing them to theoretical results published in [2]. The same assumptions made in [2] were applied to the rotational inertia matrices (Eqs. (38-41)). These have been shown to be consistent with the previous results in Figures 26-29 and are summarised as follows:

- Gyroscopic effects were assumed to come only from shaft and disk, i.e. the gyroscopic effect from the blade inertia was ignored in [2].

- The disk was assumed to be rigid in [2].

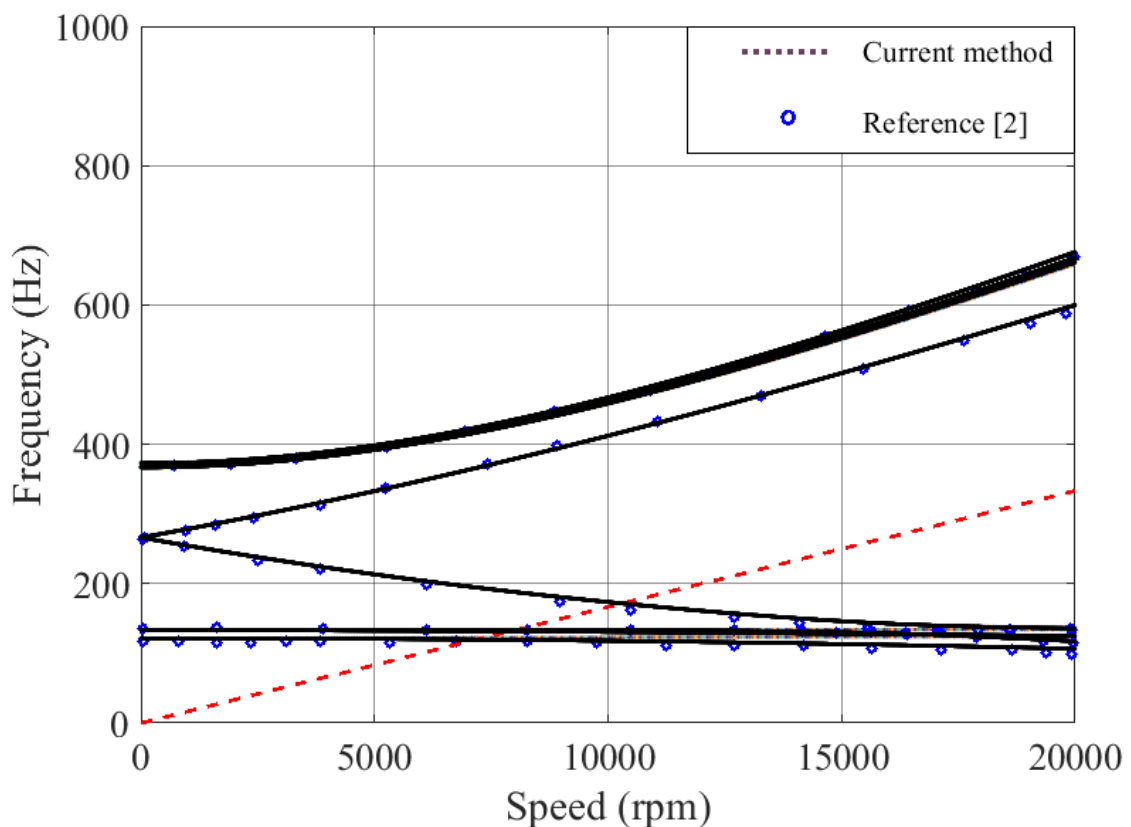- Centrifugal stiffening and spin-softening effects were assumed to come only from the blades in [2].

Fig. 30. Example 4 - Campbell diagram with all rotational effects included.

The resulting Campbell diagram in Fig. 30 is found to be in a good agreement with that published in [2].
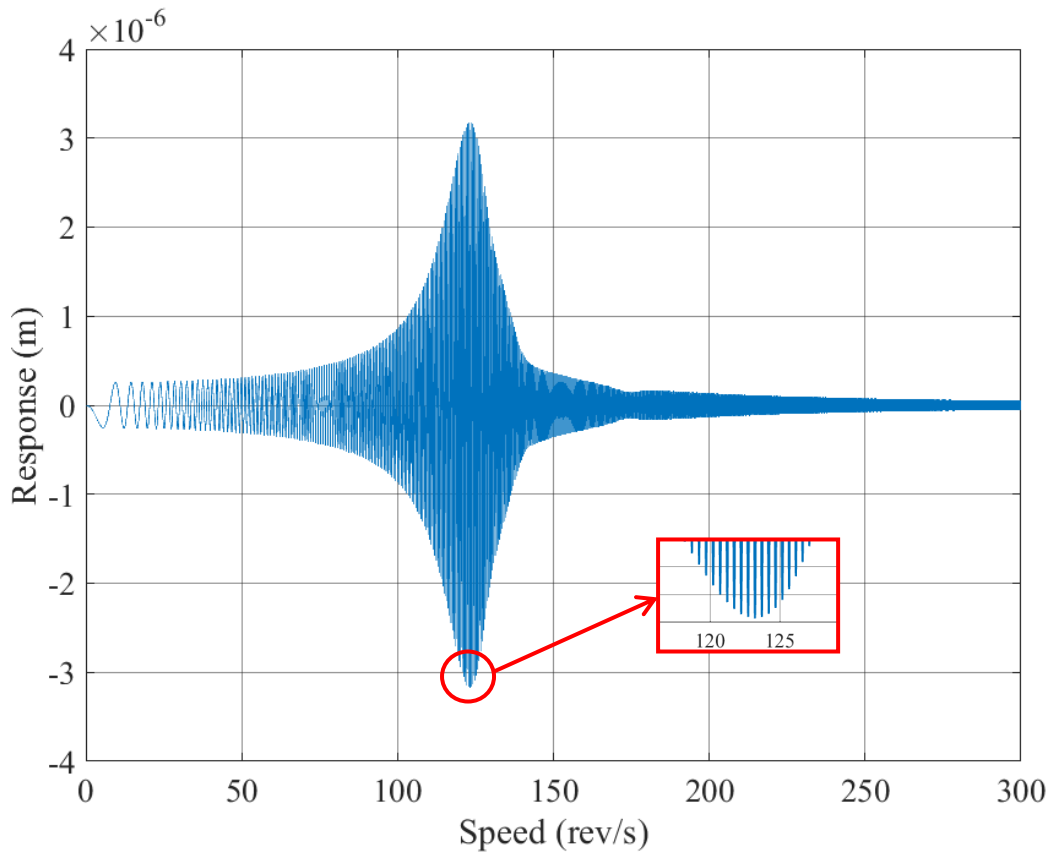
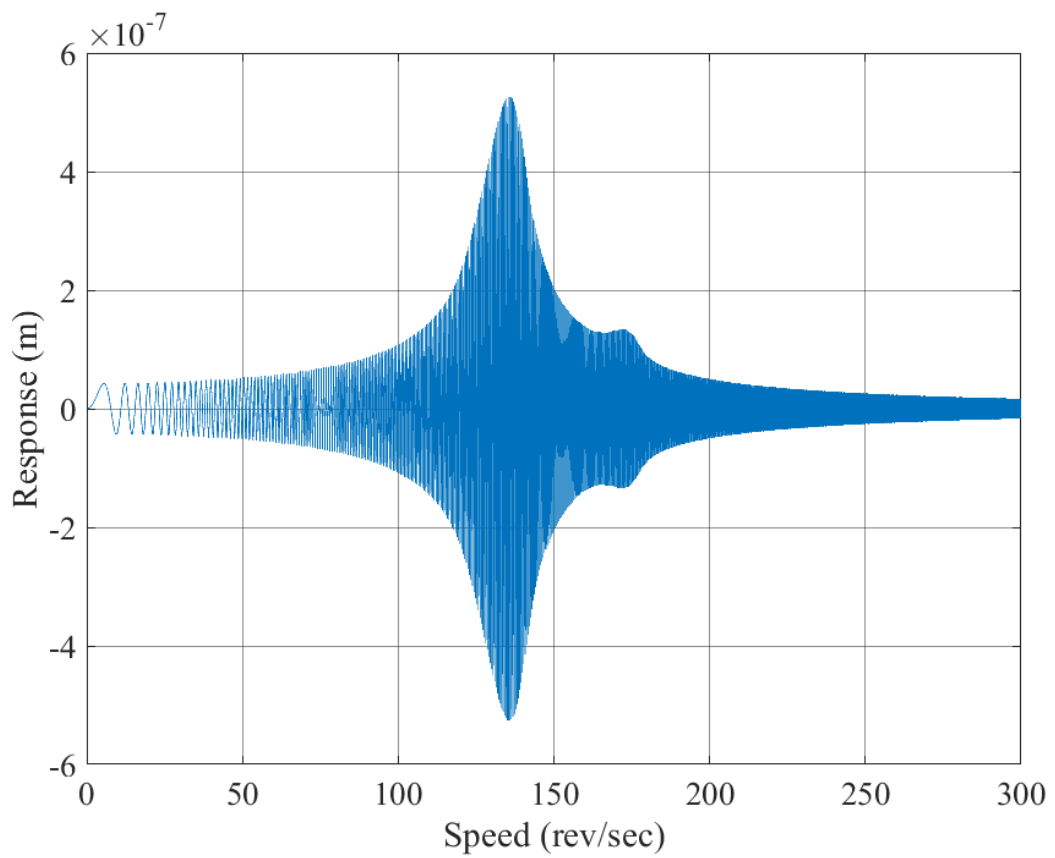Fig. 31. Forced response (first critical speed)

Fig. 32. Forced response (second and third critical speeds)

The Campbell diagram in Fig. 30 was generated in just 1 or 2 minutes, depending on how many speed steps were required. To do the same analysis with *ANSYS* rotordynamics solver, the PRESTRESS command should be used for centrifugal stiffening and spin softening, and CORIOLIS command should be activated in modal analysis for the gyroscopic effect. Such an analysis was found to take a very long time, since it required, for each speed value, a separate analysis to generate the solution. This further validates the new method proposed in this paper.
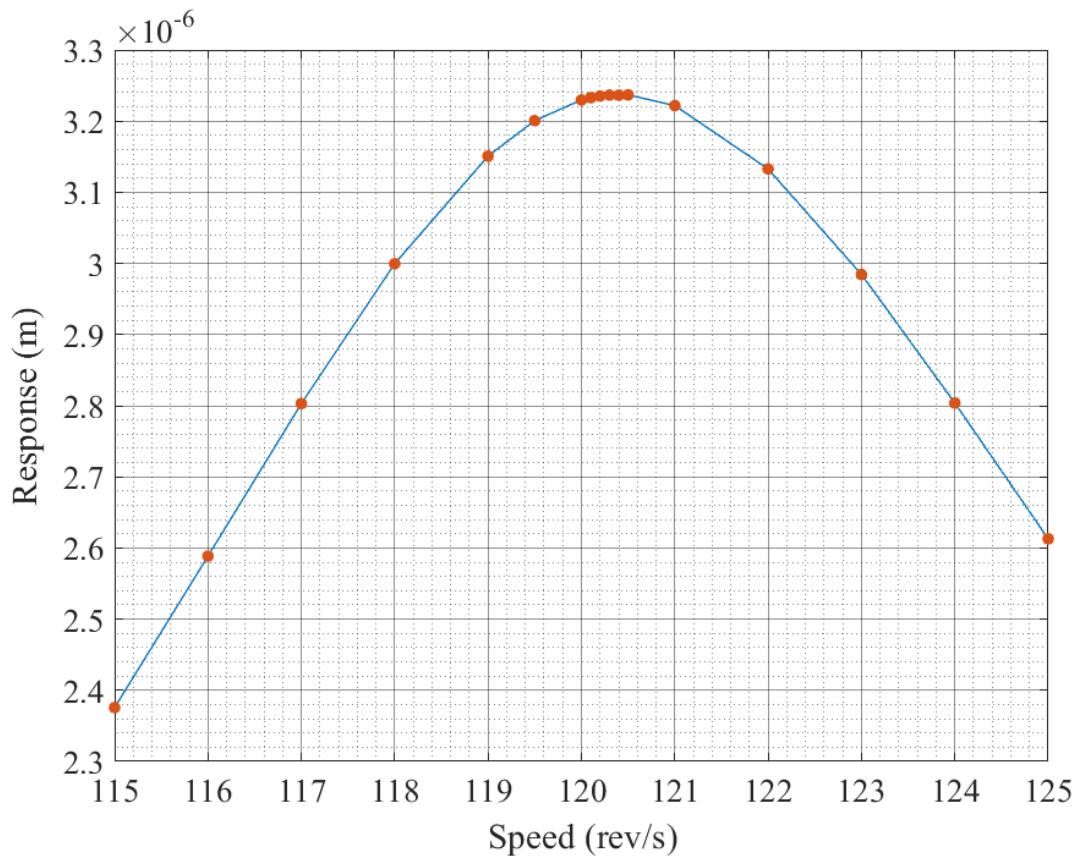

Fig. 33. Steady state Forced response around the first critical speed

The critical speeds with respect to a 1 EO excitation (i.e. EO = 1, Eq. (56)), are identified in Fig. 30 and presented in Table 11.

Table 11: Critical speeds (1 EO excitation) for Campbell diagram of Fig. 30

Mode #	1	2	3
Critical speed (rev/sec)	120.15	133.5	171.7

Fig. 31 and Fig. 32 show the forced responses at two different blades tips in x-direction due to a chirp excitation at one of the blades tips nodes (normal to the blade) under variable speed condition, as per Eq. (56) with $A = 1$ and $EO = 1$ and $T_s = 5$ sec , $\zeta_r = 0.05$ (Eq. (5)). The resonance frequencies agree with the critical speeds listed in Table 11. However, there are slight errors in their values, since the response is transient and not strictly steady-state. In order to confirm that, the simulation was repeated at a number of fixed speed values Ω_k around the first critical speed (i.e. in Eq. (56), $\Omega_i = \Omega_f = \Omega_k$) so that the system reaches steady-state for each Ω_k. The results are plotted in Fig. 33 for first critical speed, confirming the agreement between the forced response and the Campbell diagram.

CONCLUSIONS

This paper has introduced a novel methodology to include rotational effects (centrifugal stiffening, Coriolis forces, spin softening and gyroscopic moments) in a generic shaft-blisk system, using zero-speed modal data. The method does not require additional FE analysis at each speed or the derivation of equations from first principles. This research was motivated by the need to upgrade a shaft-blisk simulator designed to generate blade tip timing (BTT) data for the development and validation of BTT algorithms. To ensure computational efficiency, the dynamic response of the existing simulator was governed by modal equations based on the eigenvectors and eigenvalues of the FE analysis at zero-rotational speed. The upgraded simulator equations remained based on the same speed-independent eigenvectors

since the rotation-induced inertia effects were introduced as "external" excitations at discrete locations. The methodology was progressively validated using six examples, its accuracy checked against results from the literature and commercial software. A notable observation is the high computational speed in generating a Campbell diagram for gyroscopic effects on a flexible disk, or for centrifugal effects, where the new method was found to deliver the diagram with high resolution (1000 points) over a wide speed range (0 rpm to 60000 rpm) in a few minutes, compared to a few hours taken by commercial FE rotordynamics software. Such computational speed is essential for the generation of BTT data by the simulator under forced conditions, since the process of determining the blade passing time (past a given probe) involves multiple calculations in the integration process for the forced response (including revisions in the time step) [42]. Future research will focus on the inclusion of the parametric excitation term (Eq. (55)) arising from the shaft vibration.

ACKNOWLEDGMENT

APPENDIX A

With reference to Fig. 2, the disc is divided into N_r radial segments of constant thickness, each radial segment is divided into N_a angular segments, and each blade is divided into N_{br} radial segments.

Polar moment of inertia

For the blade segment shown in Fig. A.1:
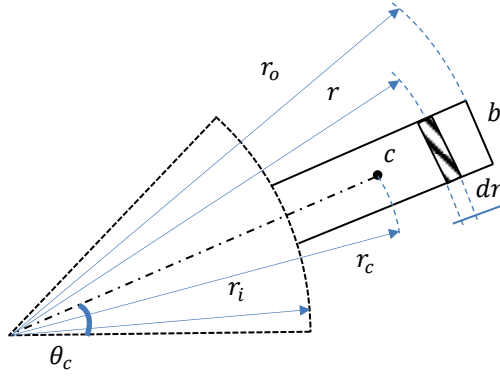
Fig. A.1. Blade division element

$$\Delta I = \int_{r_i}^{r_o} r^2 \rho t b \ dr = \rho t b \left(\frac{r^3}{3}\right)_{r_i}^{r_o} = \frac{\rho t b}{3}(r_o^3 - r_i^3)$$ (A.1)

where t, ρ are the thickness and density respectively.

Fig. A.2. Disk division

For the disc segment shown in Fig. A.2.
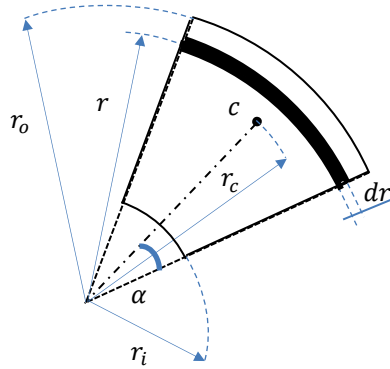
$$\Delta I = \int_{r_i}^{r_o} r^2 \ \rho t(2r\alpha) dr = 2\rho t \alpha \int_{r_i}^{r_o} r^3 \ dr = \frac{\rho t \alpha}{2}(r_o^4 - r_i^4)$$ (A.2)

Centre of mass

The position of the centre of mass of each segment (denoted by P_k in the main text) is determined by two components (angular and radial). In the case of a blade segment no. i:

$$\theta_{c_i} = \theta_{c_1} + 2\alpha_b(n_i - 1) \quad , \quad n_i = 1,2,\dots\dots, N_b \tag{A.3}$$

where θ_{c_i} is the angle of the segment no. i centre measured from the positive x−axis, θ_{c_1} is the angle of first blade, α_b is the angular difference between consecutive blades assuming that the first blade is in line with the positive x−axis, and N_b is the total number of blades. The radial position of segment centre is

$$r_{c_i} = \frac{r_i + r_o}{2} \tag{A.4}$$

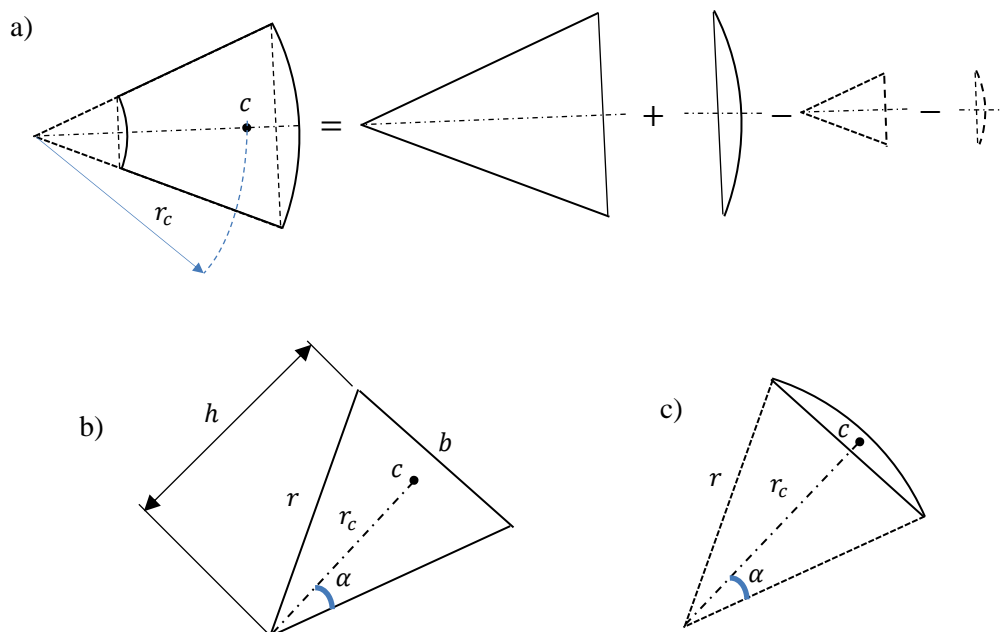Where r_i and r_o are the inner and outer radii of the segment.

Fig. A.3. Centre of mass of disk divisions

61

In the case of a disc segment no. i:

$$\theta_{c_i} = \theta_{c_1} + 2\alpha_d(n_i - 1) \quad , \quad n_i = 1,2,\ldots\ldots, N_a \tag{A.5}$$

where α_d is the angular difference between every two angular segments of the disc, and N_a is the total number of angular divisions. In order to obtain r_{c_i}, the segment is divided into 4 parts, as shown in Fig. A.3(a).

For segments 1 and 3 shown in Fig. A.3(b)

$$h = r\,\cos\alpha, \quad b = 2r\sin\alpha \qquad \alpha \text{ is half the segment angle} \tag{A.6}$$

$$A = b\,r\cos(\alpha)\,/2 = r^2\sin\alpha\cos\alpha \tag{A.7}$$

$$r_c = \frac{2}{3}r \tag{A.8}$$

For segments 2 and 4 shown in Fig. A.3(c)

$$A = \frac{1}{2}r^2(2\alpha - \sin 2\alpha) \tag{A.9}$$

$$r_c = \frac{4r(\sin\alpha)^3}{3(2\alpha - \sin(2\alpha))} \tag{A.10}$$

Finally, the radius of the segment's centre of mass is calculated as

$$r_{c_i} = \frac{A_1 r_{c_1} + A_2 r_{c_2} - A_3 r_{c_3} + A_4 r_{c_4}}{A_1 + A_2 - A_3 + A_4} \tag{A.11}$$

APPENDIX B (Table of Nomenclature)

A_1 Coriolis effect matrix

A_2 Spin softening matrix

A_3 Angular acceleration matrix

C Modal damping matrix

D Diagonal matrix containing the squares of the natural frequencies

EI The flexural rigidity of a beam

EO Engine Order

$F_{zP_k}(t)$ A harmonic force

$f(t)$ Vector of external dynamic excitation forces

G Gyroscopic effect matrix

g_k 2×1 moment vector containing the gyroscopic effect

H Number of modes used in transformation

$H_{g_k}, H_{h_k}, H_{m_k}$ Zero-speed modal matrices whose H columns are the mass-normalised eigenvectors evaluated at the degrees of freedom associated with g_k, h_k, and m_k respectively

H_P, H_f Zero-speed modal matrices.

h_k 2×1 force vector of the Coriolis and spin-softening effects

h_{0_k} 2×1 vibration-independent rotational force vector

i, j, k Unit vectors parallel to axes X, Y, Z (Fig.1)

i', j' Unit vectors parallel to U, V (Fig. 1)

$i^{(in)}, j^{(in)}$ Unit vectors parallel to axes $X^{(in)}$, $Y^{(in)}$ (Fig. 1)

L Beam length

L_k Angular momentum of a segment with mass centre P_k

M_{zP_k}, M_{vP_k} Induced moments in the edge-wise (UV) and flap-wise (UZ) planes due to the centrifugal tension N_{P_k}

m Mass per unit length

m_k A 3×1 moment vector of the centrifugal stiffening effect

N Centrifugal stiffening matrix

N_{P_k} The centrifugal tension on a segment with mass centre P_k of radial extent ΔR_{P_k}

$n_{def_k}(t)$ The variable part of n_k due to its change in direction

n_k	A unit vector originally parallel to k
Q_{cr}	The critical buckling load of the cantilever
$q(t)$	The $H \times 1$ vector of modal coordinates
R, R_{P_k}	radial coordinate of P, P_k in rotating frame XY (Fig. 1, 2)
r	The position vector of an arbitrary point P´ that was at P prior to deformation
s	State vector
T	2×2 coordinate transformation matrix (eq. (6c))
T_{aug}	Augmented form of T for all degrees of freedom in a vector
T_s	Duration
u, v	Deflections of P in UV frame (Fig. 1, 2)
$u(t)$	$3N \times 1$ vector containing the instantaneous absolute coordinates of a subset of FE nodes Q_n $(n = 1 \dots N)$
$u^{(rgd)}(t)$	The *absolute* blade tip positions due to rotation of the blisk as a rigid body
ΔI_{P_k}	The moment of inertia of the segment about the nominal axis of rotation OZ
Δm_{P_k}	The mass of the segment with mass centre at P_k (Fig. 2)
$\Delta u^{(def)}(t)$	Dynamic response to excitation (eq. (1))
$\Delta u^{(off)}(t)$	Prescribed steady shift
X, Y	Coordinates in rotating frame (Fig. 1, 2)
$X^{(in)}, Y^{(in)}$	Coordinates in inertial frame (Fig. 1, 2)
Z	Coordinate along axis of rotation
X_0, Y_0, Z_0	Coordinates of undeformed position in frame XYZ (Fig. 1)
x, y, z	Local deformations in a rotating frame
$\varphi(t)$	Rigid rotation of blisk
ζ_r	Modal damping ratio
$\vartheta, \vartheta_{P_k}$	Angular coordinate of P, P_k in rotating frame XY (Fig. 1, 2)
$\theta_x, \theta_y, \theta_z$	The angular deformations about the respective local Cartesian axes, of a vector n that is attached, and always perpendicular to, a local plane at the undeformed position of point P
λ	Eigenvalue
Ω	Angular velocity
Ω_i, Ω_f	Initial and final angular velocities

ω	Excitation frequency
ϖ_r	Undamped natural circular frequencies at $\Omega = 0, r = 1 \dots H$

REFERENCES

[1] C.-H. Yang, S.-C. Huang, Coupling Vibrations in Rotating Shaft-Disk-Blades System, Journal of Vibration and Acoustics. 129 (2007) 48–57.

[2] H. Ma, Y. Lu, Z. Wu, X. Tai, H. Li, B. Wen, A new dynamic model of rotor–blade systems, Journal of Sound and Vibration. 357 (2015) 168–194.

[3] I.Y. Shen, C.-P.R. Ku, A Nonclassical Vibration Analysis of a Multiple Rotating Disk and Spindle Assembly, Journal of Applied Mechanics. 64 (1997) 165–174.

[4] V. Omprakash, V. Ramamurti, Natural frequencies of bladed disks by a combined cyclic symmetry and Rayleigh-Ritz method, Journal of Sound and Vibration. 125 (1988) 357–366.

[5] T. Yokoyama, Free vibration characteristics of rotating Timoshenko beams, International Journal of Mechanical Sciences. 30 (1988) 743–755.

[6] S.Y. Lee, S.M. Lin, Bending Vibrations of Rotating Nonuniform Timoshenko Beams With an Elastically Restrained Root, Journal of Applied Mechanics. 61 (1994) 949–955.

[7] H. Du, M.K. Lim, K.M. Liew, A Power Series Solution For Vibration Of A Rotating Timoshenko Beam, Journal of Sound and Vibration. 175 (1994) 505–523.

[8] V.T. Nagaraj, Approximate formula for the frequencies of a rotating Timoshenko beam, Journal of Aircraft. 33 (1996) 637–639.

[9] K.B. Subrahmanyam, K.R. V. Kaza, Vibration and Buckling of Rotating, Pretwisted, Preconed Beams Including Coriolis Effects, Journal of Vibration Acoustics Stress and Reliability in Design. 108 (1986) 140–149.

[10] H.H. Yoo, S.H. Shin, Vibration Analysis of Rotating Cantilever beams, Journal of Sound and Vibration. 212 (1998) 807–828.

[11] S.C. LIN, K.M. HSIAO, Vibration Analysis of A Rotating Timoshenko Beam, Journal of Sound and Vibration. 240 (2001) 303–322.

[12] J. a Dopkin, T.E. Shoup, Rotor Resonant Speed Reduction Caused by Flexibility of Disks, Journal of Engineering for Industry. 96 (1974) 1328–1333.

[13] F. Kushner, Disc Vibration - Rotating Blade and Stationary Vane Interaction, Journal of Mechanical Design. 102 (1980) 579–584.

[14] D.R. Chivens, H.D. Nelson, The Natural Frequencies and Critical Speeds of a Rotating, Flexible Shaft-Disk System, Journal of Engineering for Industry. 97 (1975) 881–886.

[15] G. Jacquet-Richardet, G. Ferraris, P. Rieutord, Frequencies and Modes of rotating flexible Bladed Disk-Shaft Assemblies: A Global Cyclic Symmetry Approach, Journal of Sound and Vibration. 191 (1996) 901–915.

[16] E.F. Crawley, E.H. Ducharme, D.R. Mokadam, Analytical and Experimental Investigation of the Coupled Bladed Disk/Shaft Whirl of a Cantilevered Turbofan, Journal of Engineering for Gas Turbines and Power. 108 (1986) 567.

[17] A.A.S. Shahab, J. Thomas, Coupling effects of disc flexibility on the dynamic behaviour of multi disc-shaft systems, Journal of Sound and Vibration. 114 (1987) 435–452.

[18] S.-B. Chun, C.-W. Lee, Vibration Analysis of Shaft-Bladed Disk System by Using Substructure Synthesis and Assumed Modes Method, Journal of Sound and Vibration. 189 (1996) 587–608.

[19] R. Venkatachalam, S.B. Prabu, Vibration characteristics of orthotropic shaft–disk system with different constrained damping layers: experimental and numerical study, The International Journal of Advanced Manufacturing Technology. 65 (2013) 601–610.

[20] Y.-Q. Yin, B. Zhang, Y. Li, W.-Z. Lu, Effect of Dead Load on Dynamic Characteristics of Rotating Timoshenko Beams, Mathematical Problems in Engineering. 2015 (2015) 1–10.

[21] H. Ma, F. Yin, Z. Wu, X. Tai, B. Wen, Nonlinear vibration response analysis of a rotor-blade system with blade-tip rubbing, Nonlinear Dynamics. 84 (2016) 1225–1258.

[22] Y.-J. Chiu, X.-Y. Li, Y.-C. Chen, S.-R. Jian, C.-H. Yang, I.-H. Lin, Three methods for studying coupled vibration in a multi flexible disk rotor system, Journal of Mechanical Science and Technology. 31 (2017) 5219–5229.

[23] R.L. Eshleman, R.A. Eubanks, On the Critical Speeds of a Continuous Shaft-Disk System, Journal of Engineering for Industry. 89 (1967) 645–652.

[24] M. Sakata, K. Kimura, S.K. Park, H. Ohnabe, Vibration of bladed flexible rotor due to gyroscopic moment, Journal of Sound and Vibration. 131 (1989) 417–430.

[25] M. Shahgholi, S.E. Khadem, S. Bab, Nonlinear vibration analysis of a spinning shaft with multi-disks, Meccanica. 50 (2015) 2293–2307.

[26] V. Ruffini, C.W. Schwingshackl, J.S. Green, Prediction Capabilities of Coriolis and Gyroscopic Effects in Current Finite Element Software, in: P. Pennacchi (Ed.),

Proceedings of the 9th IFToMM International Conference on Rotor Dynamics, Springer, Cham, 2015: pp. 1853–1862.

[27] K. a Ansari, On the Importance of Shear Deformation, Rotatory Inertia, and Coriolis Forces in Turbine Blade Vibrations, Journal of Engineering for Gas Turbines and Power. 108 (1986) 319–324.

[28] R.M. Krupka, A.M. Baumanis, Bending-Bending Mode of a Rotating Tapered-Twisted Turbomachine Blade Including Rotatory Inertia and Shear Deformation, Journal of Engineering for Industry. 91 (1969) 1017–1024.

[29] F. Sisto, A. Chang, M. Sutcu, The Influence of Coriolis Forces on Gyroscopic Motion of Spinning Blades, Journal of Engineering for Power. 105 (1983) 342–347.

[30] N. Khader, R.G. Loewy, Shaft flexibility effects on the forced response of a bladed-disk assembly, Journal of Sound and Vibration. 139 (1990) 469–485.

[31] J. Xin, J. Wang, Investigation of Coriolis Effect on Vibration Characteristics of a Realistic Mistuned Bladed Disk, in: ASME. Turbo Expo: Power for Land, Sea, and Air, Volume 6: Structures and Dynamics, Parts A and B, Vancouver, British Columbia, Canada, 2011: pp. 993–1005.

[32] V. Ruffini, C. Schwingshackl, J. Green, Experimental and Analytical Study of Coriolis Effects in Bladed Disk, in: ASME. International Design Engineering Technical Conferences and Computers and Information in Engineering Conference, Volume 8: 27th Conference on Mechanical Vibration and Noise, Boston, Massachusetts, USA, 2015: p. V008T13A070.

[33] X. Kan, Z. Xu, B. Zhao, J. Zhong, Effect of coriolis force on forced response magnification of intentionally mistuned bladed disk, Journal of Sound and Vibration. 399 (2017) 124–136.

[34] J.S. Przemieniecki, Theory of Matrix Structural Analysis., McGraw-Hill, New York, 1985.

[35] V. Ramamurti, R. Kielb, Natural frequencies of twisted rotating plates, Journal of Sound and Vibration. 97 (1984) 429–449.

[36] J.R. Banerjee, Free Vibration of Centrifugally Stiffened Uniform and Tapered Beams Using the Dynamic Stiffness Method, Journal of Sound and Vibration. 233 (2000) 857–875.

[37] J.R. Banerjee, Dynamic Stiffness Formulation and Free Vibration Analysis of Centrifugally Stiffened Timoshenko Beams, Journal of Sound and Vibration. 247 (2001) 97–115.

[38] J.R. Banerjee, Dynamic stiffness formulation for structural elements: A general approach, Computers & Structures. 63 (1997) 101–103.

[39] Y. Chen, J. Zhang, H. Zhang, X. Li, J. Zhou, Extraction of Natural Frequencies and Mode Shapes of Rotating Beams by Variational Iteration Method, International Journal of Structural Stability and Dynamics. 16 (2016) 1450106.

[40] P. Kohnke, Theory Reference for the Mechanical APDL and Mechanical Applications, 12th ed., ANSYS, Inc., Canonsburg, PA, USA, 2009.

[41] M. Mohamed, P. Bonello, P. Russhard, An Experimentally Validated Modal Model Simulator for the Assessment of Different Blade Tip Timing (BTT) Algorithms, Mechanical Systems and Signal Processing. (Under rev (n.d.).

[42] M. Mohamed, P. Bonello, P. Russhard, The Determination of Steady-State Movements Using Blade Tip Timing Data, in: ASME. Turbo Expo: Power for Land, Sea, and Air, Volume 7C: Structures and Dynamics, ASME, Oslo, Norway, 2018: p. V07CT35A010.

[43] F. Figaschewsky, B. Hanschke, A. Kühhorn, Efficient Generation of Engine Representative Tip Timing Data Based on a Reduced Order Model for Bladed Rotors, Journal of Engineering for Gas Turbines and Power. 141 (2018) 012503.

[44] I.F. Santos, C.M. Saracho, J.T. Smith, J. Eiland, Contribution to experimental validation of linear and non-linear dynamic models for representing rotor-blade parametric coupled vibrations, Journal of Sound and Vibration. 271 (2004) 883–904. doi:10.1016/S0022-460X(03)00758-2.

[45] M. Mohamed, P. Bonello, P. Russhard, A novel method for the determination of the change in blade tip timing probe sensing position due to steady movements, Mechanical Systems and Signal Processing. 126 (2019) 686–710.

[46] Ordinary Differential Equations, MATLAB R2019a. (2019). https://uk.mathworks.com/help/matlab/ordinary-differential-equations.html?s_tid=CRUX_lftnav (accessed July 1, 2019).

[47] F.J. Shaker, Effect of Axial Load on Mode Shapes and Frequencies of Beams, in: NASA Technical Note, NASA TN D-8109, Lewis Research Center, 1975.

[48] W. Zhang, W. Wang, H. Wang, J. Tang, Analytical and experimental investigation of bladed-disk/shaft coupled system, in: Proceedings of the Fourth International Conference on Rotor Dynamics, 1994: pp. 63–68.

[49] R.D. Blevins, Formulas for natural frequency and mode shape, Van Nostrand Reinhold, New York ;, 1979.

[50] R.C. Hibbeler, Mechanics of materials, 7th ed., Pearson Prentice Hall, Upper Saddle River, N.J, 2008.

[51]   J. Strnad, J. Liska, Diagnostic methods of a bladed disc mode shape evaluation used for shrouded blades in steam turbines, Journal of Physics: Conference Series. 659 (2015) 012051.